Friedrich-Wintgen bound states in the continuum in a photonic and plasmonic T-shaped cavity: Application to filtering and sensing

Soufyane Khattou ,[1] Yamina Rezzouk,[1] Madiha Amrani,[1] Mohamed El Ghafiani ,[1]
El Houssaine El Boudouti ,[1,*] Abdelkrim Talbi ,[2] and Bahram Djafari-Rouhani [3]

[1] *LPMR, Département de Physique, Faculté des Sciences, Université Mohammed I, Oujda, Morocco*

[2] *Univ. Lille, CNRS, Centrale Lille, Université Polytechnique Hauts-de-France, UMR 8520-IEMN, LIA LICS, Lille 59000, France*

[3] *IEMN, UMR CNRS 8520, Département de Physique, Université de Lille, Villeneuve d'Ascq 59655, France*

Bound states in the continuum (BICs) in open cavities have attracted considerable attention in wave physics due to their ability to confine light and produce high-quality-factor resonances with promising applications for filtering and sensing. One of the most interesting types of BICs is Friedrich-Wintgen (FW) BICs, which result from destructive interference of two interacting modes belonging to the same radiation channel. Here, we investigate theoretically and experimentally FW BICs in a photonic and plasmonic T-shaped cavity made of two horizontal guides of lengths d_2 and d_3 coupled to a vertical stub of length d_1. We demonstrate that the necessary condition for obtaining BICs consists in taking the lengths of the two horizontal guides d_2 and d_3 commensurate. This BIC is a common mode of the guides of lengths d_2 and d_3, such as the electric field vanishes at their connection point with the stub of length d_1; this BIC is independent of d_1 and the infinite waveguide to which the whole cavity will be attached. We show that, depending on d_1, the FW BIC appears as the consequence of the interaction between two eigenmodes of the originally isolated cavity where the width of one mode vanishes giving rise to FW BIC, while the width of the second mode becomes broad. In addition, we show that by slightly deviating from the BIC condition, the latter transforms to either electromagnetically induced transparency (EIT) or reflection or Autler-Townes splitting (ATS) resonances. Both EIT and ATS effects are qualified as a transparency window between two transmission zeros, but with different physical origins. We exploit the Akaike's information criterion test to discern EIT from ATS and distinguish the regime where the EIT or ATS effect dominates. The theoretical results, obtained by means of the Green's function method, are validated both by experimental measurements using coaxial cables in the radiofrequency domain and numerical simulations using metal-insulator-metal plasmonic waveguides operating in the infrared domain. The sensitivity of the PIT (the plasmonic analogue of EIT) resonances to the dielectric inside the waveguides can be used to design a highly sensitive sensor, which makes it suitable for an on-chip optical sensing platform.

I. INTRODUCTION

An open cavity system is characterized by its resonances, which are the consequence of the interaction of its discrete states with the continuum of states of the surrounding media. The finite width of the resonances is a characteristic of the open system, associated with the energy leakage from the system to outside. The width and spectral position of the resonances are related to the imaginary and real parts of the complex eigenfrequencies of the cavity. When the width of the resonances is reduced to zero, the resonant (or leaky) mode transforms into a bound state in the continuum (BIC) without radiating energy away [1].

The concept of BIC has been predicted one century ago by von Neumann [2] in a special quantum well system. In recent years, BICs have been intensively studied theoretically and experimentally in various classical systems, such as photonic [3–5], plasmonic [6,7], and acoustic systems [8–10]. Due to their high-quality factors, BICs have known potential applications in filtering, sensing, lasing, and nonlinear optics [11,12]. Generally, the BICs can occur through different mechanisms depending on their physical origin, such as Fabry-Perot (FP) BICs [13], symmetry protected (SP) BICs [14–16], and Friedrich-Wintgen (FW) BICs [17–23]. FP BICs refer to destructive interference when the spacing between two resonant cavities is tuned to make the round-trip phase shift add up to an integer multiple of 2π [13]. SP BICs refer to symmetry incompatibility

---
*Corresponding author. elboudouti@yahoo.fr

between two sets of modes, namely a bound state with one symmetry class may fall in a continuum state with another class of symmetry without any coupling between them [14–16]. Finally, FW BICs result from the destructive interference of two resonant modes belonging to the same cavity. The two modes approach each other as a function of a certain continuous parameter, their interference induces an avoided crossing of the two resonances, and at a specific value of the parameter, the width of one resonance vanishes giving rise to a FW BIC, while the other resonance becomes more lossy with a maximal width [17–23]. In addition, when the system is slightly detuned from the BIC condition, the latter transforms in general to a quasi-BIC in the shape of a Fano [24,25] or electromagnetically induced transparency (EIT) [26], or reflection (EIR) [27] or Autler-Townes splitting (ATS) [28] resonances with a finite width. The Fano resonance is characterized by a resonance near to an anti-resonance with an asymmetric line shape in the transmission spectra, while EIT (EIR) appears as a resonance squeezed between two transmission (reflection) zeros. However, ATS exhibits similar spectral features as EIT but with a different physical origin [29]. The advantage of the latter resonances in comparison with the usual Breit-Wigner (or Lorentzian) resonance [30] lies in the fact that one can control their linewidths and obtain resonances with high-quality factors for certain geometrical parameters.

The performance of sensors are essentially related to their ability to detect material changes in the surrounding medium. Different characteristics are used to evaluate the performance of a sensor such as the sensitivity (S), figure of merit (FOM), and detection limit (DL) [31]. A good sensor is characterized by a high sensitivity and narrow resonance, high FOM, and low DL. Therefore, to achieve a good sensor it is preferable to exploit the property of BICs and quasi-BIC resonances, which are characterized by narrow resonances and high-quality factors. The BIC appears as a zero linewidth resonance, therefore it is necessary to transform it into a quasi-BIC in the shape of a Fano or EIT resonance with a certain width to be used in sensing application [31]. Within this field, BICs and quasi-BIC are widely used for sensing applications in dielectric [32–36], metallic [37,38] and hybrid metal-dielectric devices [39–41]. Metal-insulator-metal (*M-I-M*) plasmonic waveguides have been also widely used for refractive-index sensing applications in a variety of resonators with promising applications in biological and chemical fields [42–49]. The advantage of *M-I-M* plasmonic sensors in comparison with dielectric devices lies in the fact that they can present high-sensitivity values, low cost, and integration capability, however they suffer from lower FOM due to the losses in metal [31,41]. Silver (Ag) and gold (Au) are the metals used the most in the near-infrared and visible frequency domains. Ag has lower intrinsic losses compared to Au, meaning it has

lower absorption and scattering of light. However, Ag is more prone to oxidation and can exhibit higher losses due to surface roughness, which requires some treatment during the fabrication process [50]. Au is more chemically stable and easier to work with in terms of fabrication, and can be an option in this frequency range. Recently, several *M-I-M* plasmonic devices based on stubs and nanocavities using Au have been designed and experimentally implemented to observe EIT and Fano resonances [42,51–53]. Also, Kamada *et al.* [54] have used Ag to design and fabricate a compact unbalanced Mach-Zehnder interferometer (MZI) based on *M-I-M* plasmonic waveguides. The MZI was fabricated by a lithography technique and provides an experimental realization of the transmission performance of the MZI using *M-I-M* waveguides.

In open cavities, one of the well-known BICs is FW type, which results from the destructive interference of two resonant modes associated with the same cavity. Recently, FW BICs have been studied in an acoustic T-shaped cavity [9] and a photonic loop laterally coupled to a waveguide [19]. In plasmonics, a T-shaped cavity has been designed to study PIT (the plasmonic analogue of EIT resonance) resonances and band-stop filters in simple [55–57] and periodic [58] plasmonic nanodevices. Also, the T-shaped cavity has been recently proposed for sensing application in plasmonic waveguides based on bulk Dirac semimetals [55] and *M-I-M* waveguides [59,60]. However, an analytical and experimental demonstration of FW BICs in a photonic and plasmonic T-shaped cavity with an application for gas sensing and biosensing in the infrared domain has not been treated before. The geometry studied in this paper is schematically presented in Fig. 1(a).

Some years ago [61,62], we have shown that a simple structure made of two stubs of lengths d_2 and d_3 grafted at the same site along a waveguide may exhibit BICs by taking the lengths d_2 and d_3 commensurate. The BICs are found as the result of destructive interference between the modes of the two stubs with no coupling (or Rabi splitting $\kappa = 0$). Here, we show that by considering a T-shaped cavity made of a vertical guide of length d_1 coupled to the connection point of two horizontal guides of lengths d_2 and d_3 [Fig. 1(a)], one can obtain FW BICs with either no coupling or coupling regimes depending on d_1. The cavity is grafted between two semi-infinite waveguides [Fig. 1(a)] to measure the transmission and reflection coefficients. First, we give a detailed analytical calculation of the transmission and reflection coefficients and eigenmodes of the structure as well as the conditions for obtaining FW BICs. We demonstrate analytically that the necessary condition for BIC's existence, consists in taking d_2 and d_3 commensurate. In addition, we show that by slightly shifting from the BIC condition, this latter transforms into either EIT-EIR or ATS resonances with a finite width. To discern EIT from ATS effect, we first fit the transmission data using two different fitting models corresponding to
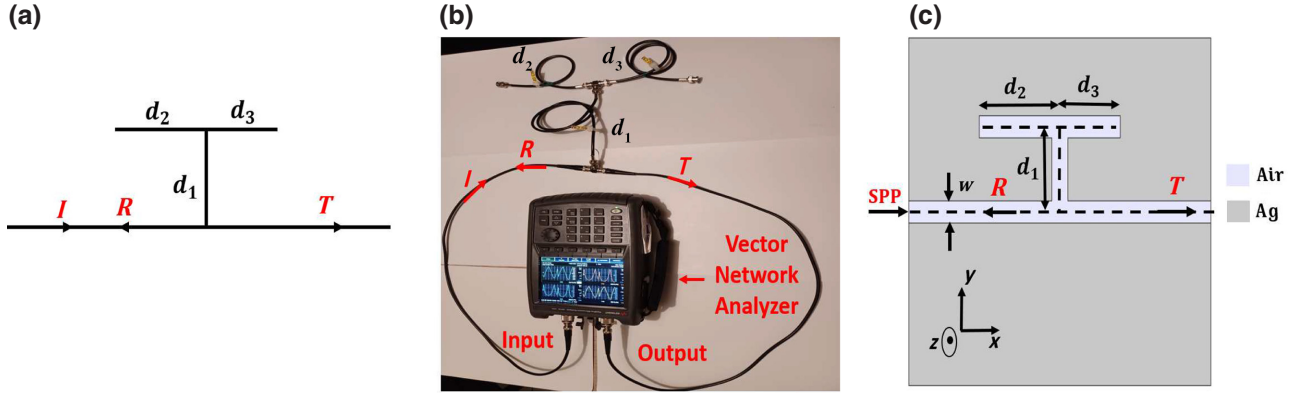
FIG. 1.   (a) Photonic T-shaped cavity made of two horizontal guides of lengths d_2 and d_3 coupled to a vertical guide of length d_1. The whole cavity is inserted between two semi-infinite waveguides. I, R, and T denote the incident, reflected, and transmitted waves, respectively. (b) Experimental setup based on coaxial cables and vector network analyzer. (c) Plasmonic T-shaped cavity based on M-I-M plasmonic waveguides of lengths d_1, d_2, and d_3. $w = 50$ nm is the width of the waveguide. SPP designates the incident surface plasmon polariton mode. Gray and blue areas indicate metal (Ag) and insulator (air), respectively.

EIT and ATS phenomena [29,63,64]. Then, we exploit the Akaike information criterion (AIC) test [65] to select the best fitting model. Also, we give a comparison between the variation of the density of states (DOS) and the first derivative of the argument of the determinant of the scattering matrix (the so-called Friedel phase[66]). All these analytical results are confirmed experimentally using coaxial cables in the radiofrequency domain. Finally, we give another validation of our analytical results to M-I-M plasmonic waveguides with an application for gas sesning and biosensing in the infrared domain. Our design shows comparable values of sensitivity and FOM with Refs. [48,67–74]. Let us mention that most numerical studies of plasmonic refractive-index sensors have used silver as a plasmonic metal [60,70–74]. Meanwhile, some papers have employed the gold as a metal for the experimental realizations of M-I-M waveguides [51–53]. However, our analytical approach remains valid and can be used for either silver or gold plasmonic waveguides as both metals can be described by similar dielectric constant based on the Drude-Lorentz model. The proposed sensor has the advantage of being a very simple device, which can be suitable for an on-chip optical-sensing platform. The analytical calculations are developed by means of the Green's function method, while the numerical simulations are obtained using the finite-element method via COMSOL Multiphysics.

The outline of the paper is organized as follows: In Sec. II, we give the analytical calculations of transmission and reflection coefficients as well as the eigenmodes of the isolated cavity with different boundary conditions. Then, we give the analytical expressions of FW BICs. In Sec. III, we provide an experimental evidence of FW BICs and induced resonances, such as EIT, ATS, and

EIR resonances. Section IV shows the results for M-I-M plasmonic waveguides with an application for sensing. In Sec. V, we summarize the main results of this work.

II. MODEL AND ANALYTICAL RESULTS

The T-shaped cavity depicted in Fig. 1(a) consists of two guides of lengths d_2 and d_3 coupled to a vertical guide of length d_1. The whole cavity is grafted between two semi-infinite waveguides [Fig. 1(a)]. We take $d = d_2 + d_3 = 1$ as constant throughout the paper and we call $\delta = d_2 - d_3$ the detuning between the two horizontal guides, which we consider variable. The calculation method used in this work is based on the Green's function method [61,75], which enables us to deduce the different properties of the cavity such as the transmission and reflection coefficients, the eigenmodes of the isolated cavity with different boundary condition at its bottom, and DOS. For the theoretical results presented in this section, we suppose that all guides are made by the same material with an impedance Z and a dielectric constant ε but with different geometrical parameters. The boundary conditions at the end of the horizontal guides is $H = 0$ (vanishing magnetic field). It should be pointed out that the analytical model presented here is valid only for monomode circuits where the width of the waveguide is smaller enough in comparison with the wavelength and the length of the waveguides. Therefore, only the fundamental mode is considered in both coaxial cables (TEM) and M-I-M waveguides (TM_0). The advantage of monomode model lies in the ability to handle the equations analytically, which enables a deep understanding of the geometrical parameters governing the BICs and the induced resonances.

A. Transmission and reflection coefficients and eigenmodes of the structure

The transmission and reflection coefficients through the T-shaped cavity [Fig. 1(a)] are given by (see the Supplemental Material SM1 [76]) [61,75]

$$t = \frac{\tau}{\tau - j\rho} \qquad (1)$$

and

$$r = \frac{j\rho}{\tau - j\rho}, \qquad (2)$$

where τ and ρ are given by

$$\tau = 2(C_1 C_2 C_3 - S_1 S), \qquad (3)$$

and

$$\rho = S_1 C_2 C_3 + C_1 S, \qquad (4)$$

with $C_i = \cos(kd_i)$, $S_i = \sin(kd_i)$ $(i = 1, 2, 3)$, and $S = \sin(kd)$, $d = d_2 + d_3$. $k = \omega\sqrt{\varepsilon}/c$ is the wave vector, ω is the angular frequency, ε is the permittivity of the waveguide, and c is the speed of light in vacuum. From Eqs. (1) and (2), one can deduce that for a lossless system, the transmission and reflection rates verify the conservation energy law $|t|^2 + |r|^2 = 1$.

It is worth mentioning that the eigenmodes of the isolated cavities with either vanishing magnetic field ($H = 0$) called Neumann boundary condition structure (NBCS) or vanishing electric field ($E = 0$) called Dirichlet boundary condition structure (DBCS) at the bottom side of the stub of length d_1, can be deduced, respectively, from the reflection and transmission coefficients zeros when this cavity is grafted to an infinite waveguide as depicted in Fig. 1(a) [77]. Consequently, the eigenmodes of DBCS and NBCS can be deduced, respectively from vanishing the expressions of t and r [Eqs. (1) and (2)], namely

$$\tau = 0, \qquad (5)$$

and

$$\rho = 0. \qquad (6)$$

B. Conditions for BICs

The eigenmodes of the whole system in Fig. 1(a) can be obtained from the poles of its Green's function or equivalently from the denominator of the transmission and reflection coefficients [Eqs. (1) and (2)], namely

$$\tau - j\rho = 2(C_1 C_2 C_3 - S_1 S) - j(S_1 C_2 C_3 + C_1 S) = 0. \qquad (7)$$

Equation (7) is a complex quantity, its real part gives the position of the resonance in the transmission spectra, while its imaginary part is related to the width of the resonance. When both the real (i.e., τ) and imaginary (i.e., $\rho = 0$) parts vanish at the same frequency, one obtains a BIC. From Eq. (7), one can see that the BICs are common modes of the two structures DBCS [Eq. (5)] and NBCS [Eq. (6)]. From an analysis of Eqs. (3) and (4), one can show easily that the two latter equations vanish simultaneously when

$$C_2 = 0 \quad \text{and} \quad C_3 = 0, \qquad (8)$$

i.e., $kd_2 = (m_2 + 1/2)\pi$ and $kd_3 = (m_3 + 1/2)\pi$, where m_2 and m_3 are two integers. In what follows, we call $\delta = d_2 - d_3$ the detuning between the horizontal guides and $\Omega = kd/\pi$ the dimensionless frequency. Therefore, the BICs are obtained when d_2 and d_3 are chosen commensurate [i.e., $d_2/d_3 = (2m_2 + 1)/(2m_3 + 1)$] or equivalently

$$\frac{\delta}{d} = \frac{m_2 - m_3}{m_2 + m_3 + 1}, \qquad (9)$$

and the BIC frequencies are given by

$$\Omega = m_2 + m_3 + 1. \qquad (10)$$

These modes are independent on the value of d_1 and the surrounding waveguides. In what follows, we will focus on the BICs and quasi-BICs for the first mode corresponding to $m_2 = m_3 = 0$ (i.e., $\delta = 0$ and $\Omega = 1$).

III. APPLICATION TO PHOTONIC CIRCUITS: EXPERIMENTAL EVIDENCE IN THE RADIOFREQUENCY DOMAIN

In this section, we will give a numerical and experimental demonstration of the analytical results discussed in the previous section for photonic circuits in the case where the length of the vertical stub d_1 is fixed and the detuning $\delta = d_2 - d_3$ between the two horizontal guides is variable and vice versa.

A. Effect of the detuning δ between the horizontal guides

FW BICs are obtained from destructive interference of two degenerate modes associated to the same cavity. The two resonant modes approach each other as a function of a certain continuous parameter, interference induces an avoided crossing of the two resonances, and at a specific value of the parameter, the width of one resonance vanishes giving rise to a FW-BIC, and the other resonance becomes more lossy [17–23].

According to the FW model [17–19], the FW BICs occur at the crossing or anticrossing of two interacting modes associated either to NBCS or DBCS. Generally, for the T-shaped cavity FW BICs can result from the interaction between two modes of NBCS ($\rho = 0$) or two modes of

DBCS ($\tau = 0$). In the transmission spectra, when the cavity is inserted between two semi-infinite waveguides, the width of one resonance vanishes giving rise to FW BIC, while the other resonance becomes broadened (see below). In what follows, we focus on the case where the FW BICs are obtained from the interaction between two modes of DBCS around $d_1 = d$. Similar results can be obtained for two modes of NBCS around $d_1 = 0.5$, these results are given in the Supplemental Material SM2 [76]. The eigenmodes of DBCS are given by $\tau = 0$ [Eq. (3)] which can be rewritten as

$$
\tau = 2S[S_1 - C_2C_3] - 2C_2C_3 \cos\left[k\left(\frac{d_1 + d}{2}\right)\right]
$$
$$
\times \sin\left[k\left(\frac{d_1 - d}{2}\right)\right]. \quad (11)
$$

In analogy with the FW model, the second term at the right-hand side of Eq. (11) represents the coupling strength (or Rabi splitting) κ between the two DBCS modes. Two cases can be distinguished, namely $d_1 = d$ where the coupling strength vanishes and $d_1 \neq d$ where the coupling can be made strong or weak. These two cases will be the subject of the forthcoming sections.

1. Coupling regime

We start with the coupling regime between two modes of DBCS. Here, we give some analytical illustrations with experimental validations in the radiofrequency domain. All the lengths will be given in units of $d = 1$ m and the dimensionless frequency $\Omega = kd/\pi$. The experiment is carried out using standard coaxial cables with a vector network analyzer [Fig. 1(b)]. The cables are connected by standard BNC T connectors of around 2 cm, which defines a limit on the variation of the cable lengths. Because of this constraint, we can achieve the experiment by a step of 5 cm. This limit enables also the different resonances and antiresonances to be distinguished better in the transmission experimental spectra. In the experiments, we have realized ten spectra for fixed d_1 (respectively, δ) and different values of δ (respectively, d_1) by a step of 10 cm (see below). The attenuation in the coaxial cables was simulated by introducing a complex dielectric permittivity $\varepsilon = \varepsilon' + j\varepsilon''$ and adding two cables at the input and output of the system that connect the T cavity to the network analyzer [see Fig. 1(b)]. These cables introduce additional attenuation in the transmission spectra. The attenuation coefficient α'' can be expressed as $\alpha'' = \varepsilon''\omega/c\sqrt{\varepsilon'}$. On the other hand, the attenuation specification data supplied by the manufacturer of the coaxial cables based on energy decreasing of the waves along the cables in the frequency range of 10–200 MHz, can be approximately fitted with the expression $ln(\alpha'') = \gamma + \beta ln(\omega)$, where γ and β are

two constants. From this fitting procedure, a useful expression for ε'' as a function of frequency can be obtained under the form $\varepsilon'' = (f/f_0)^{-0.5}$, where the frequency f is expressed in Hz and $f_0 = 9200$ Hz. The scattering matrix S of the structure was measured in the frequency range 1–200 MHz by means of a broadband vector network analyzer (VNA) Agilent PNA-X N5242A. The VNA allows accurate forward and reverse measurements on the device under test, which are needed to characterize all the four S parameters. For more details about the experimental procedure, see Refs. [61,78]. According to Eq. (11), to obtain a coupling between two modes of DBCS we should take $d_1 \neq d$. For this reason, we choose $d_1 = 0.8$. Figure 2(a) gives the dispersion curves as a function of δ for NBCS ($\rho = 0$, pink curves) and DBCS ($\tau = 0$, cyan curves). The pink and cyan circles give the experimental eigenmodes for NBCS and DBCS obtained, respectively, from the maxima and minima of the transmission coefficient in Fig. 2(b). It can be seen an avoided crossing between two modes of DBCS with $\kappa = 0.187$. Also, the appearance of a FW BIC at the intersection of one branch of NBCS and one branch of DBCS at $\delta = 0$ and $\Omega = 1$. This BIC corresponds to $m_2 = m_3 = 0$ in Eqs. (9) and (10). Figure 2(b) shows some transmission spectra as a function of Ω for some values of δ. Red and blue curves give the theoretical transmission without and with loss, respectively, while green open circles give the experimental measurements. The experiment reproduces very well the theoretical results. As a function of δ, one can see an anticrossing between two transmission dips (indicated by vertical arrows) around $\Omega = 1$ and $\delta = 0$. The width of the lower dips decreases as δ decreases until it vanishes ($\gamma_- = 0$) giving rise to a FW BIC at $\delta = 0$, while the width of the upper dip becomes maximal at the anticrossing point ($\gamma_+ = 0.26$). When we shift from the BIC position ($\delta \neq 0$), one can obtain an asymmetric transparency window between two transmission zeros, its width depends on the value of δ. For $\delta = 0.1$ [Fig. 2(b)], the resonance appears as an asymmetric EIT resonance. Its width increases as a function of δ and transforms to a resonance with a broad width for $\delta = 0.5$. The behavior of FW BIC is also shown in the transmission coefficient in color scale in Fig. 2(c). One can see a FW BIC (indicated by a cyan circle) at $\delta = 0$ and $\Omega = 1$. By slightly shifting from $\delta = 0$, the BIC transforms into an asymmetric resonance between two transmission dips. A similar behavior is obtained for negative values of δ (i.e., when we permute the two guides of lengths d_2 and d_3) as the guides d_2 and d_3 play the same role. To explain better the evolution of the linewidth of the two dips, we display in Fig. 2(d) the FWHM for the lower (red curve) and upper (blue curve) dips as a function of δ. These FWHM are obtained from the transmission spectra in Fig. 2(b). One can notice that the linewidth of the lower dip (γ_-) decreases as δ goes to zero and vanishes at $\delta = 0$ giving rise to a FW BIC with no loss ($\gamma_- = 0$). In contrast, the FWHM of the upper dip (γ_+) increases as δ decreases
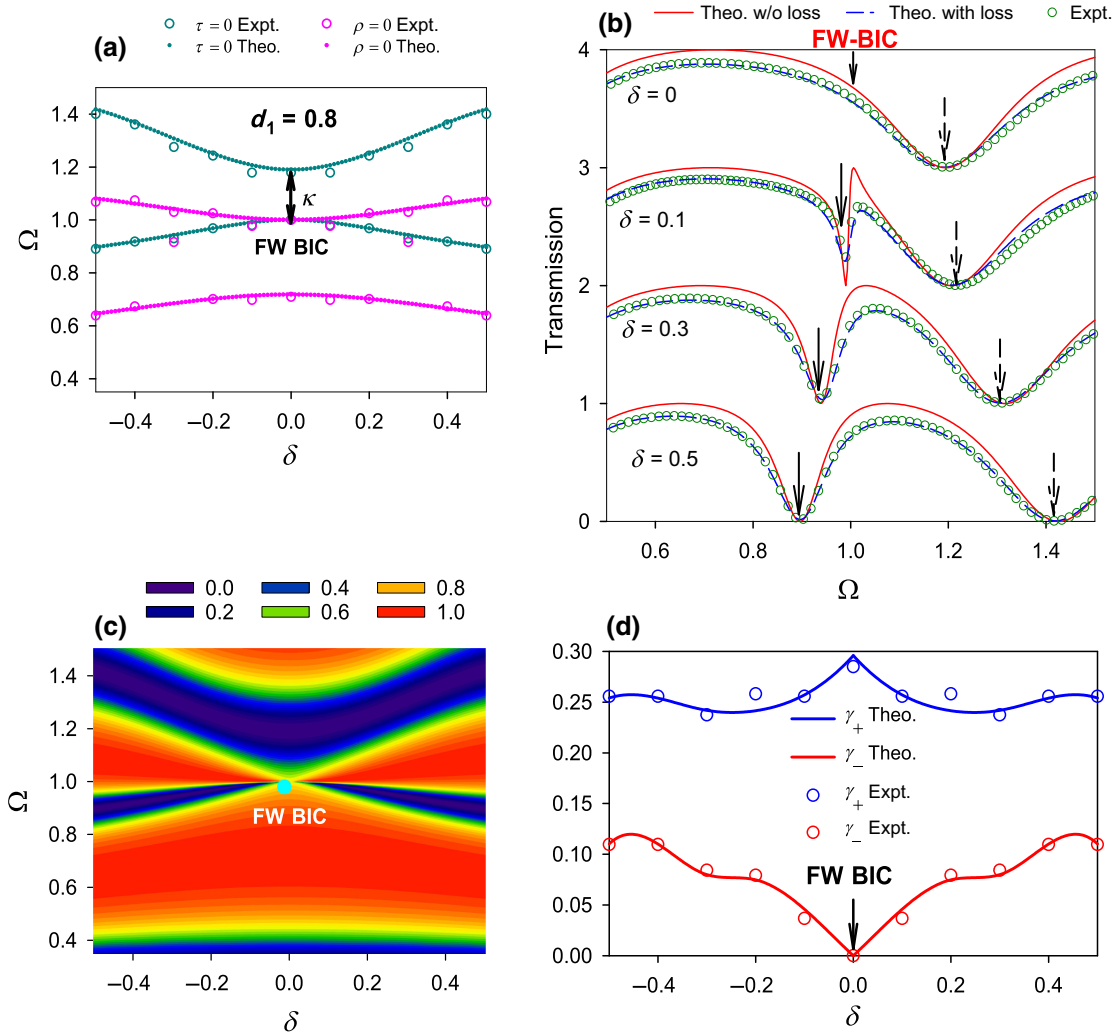
FIG. 2. (a) Dispersion curves of the system depicted in Fig. 1 with NBCS ($\rho = 0$, pink curves) and DBCS ($\tau = 0$, cyan curves) as a function of δ for $d_1 = 0.8$. $\delta = d_2 - d_3$ is the detuning between the horizontal guides of lengths d_2 and d_3. Pink and cyan circles give the experimental eigenmodes for NBCS and DBCS obtained from the maxima and minima of the transmission coefficient in (b), respectively. (b) Transmission spectra for some values of δ. Red and blue curves give the theoretical transmission without and with loss, respectively, while green open circles give the experimental measurements. The arrows indicate the frequencies of the transmission minima associated to two DBCS modes. (c) Variation of the theoretical transmission (in color scale) as a function of Ω and δ for $d_1 = 0.8$. Cyan circle indicates the FW BIC position. (d) Linewidth of the lower (red curve) and upper (blue curve) transmission dips indicated by arrows in (b). Open circles give the experimental measurements.

and becomes maximal ($\gamma_+ = 0.26$) for $\delta = 0$. The behavior of the widths γ_- and γ_+ of the two interacting modes in Fig. 2(d) is a characteristic of FW BIC [17].

2. No coupling regime

Equation (11) shows that for $d_1 = 1$ there is a decoupling between two modes of DBCS (i.e., $\kappa = 0$), namely

$$S = 0 \tag{12}$$

and

$$S_1 - C_2 C_3 = 0. \tag{13}$$

In this case, the two solutions of Eqs. (12) and (13) around $\Omega = 1$ can be written simply as

$$\Omega_\pm = (1 \pm \delta)^{-1}. \tag{14}$$

Equation (14) shows that for $\delta = 0$, the two DBCS branches cross each other at $\Omega = 1$ giving rise to two degenerate modes with no coupling strength $\kappa = 0$. For $\delta \neq 0$, one obtains two decoupled modes, the separation between them depends on δ as follows:

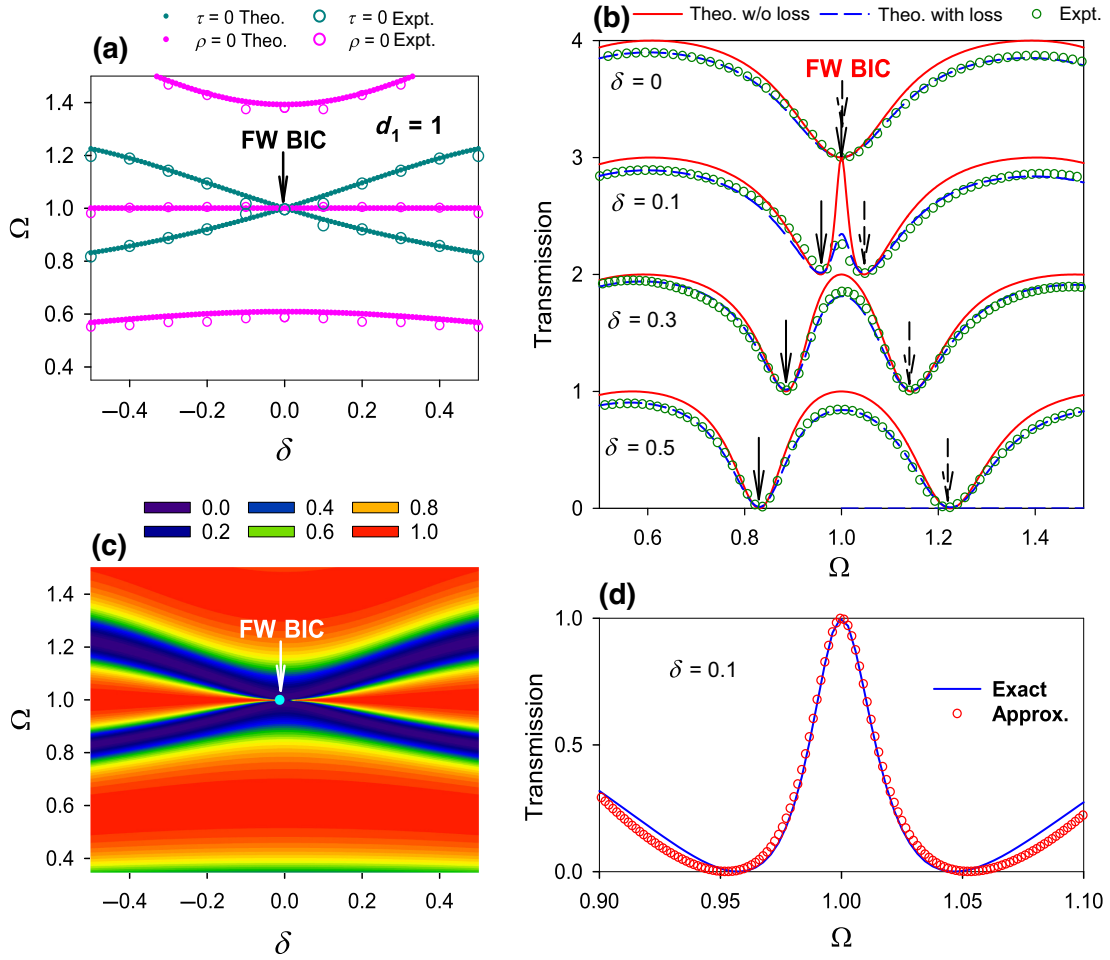$$\Delta\Omega = \Omega_+ - \Omega_- = \frac{2\delta}{1 - \delta^2}. \tag{15}$$

FIG. 3. (a) Dispersion curves of the system depicted in Fig. 1 with NBCS ($\rho = 0$, pink curves) and DBCS ($\tau = 0$, cyan curves) as a function of δ for $d_1 = 1$. Pink and cyan circles give the experimental eigenmodes for NBCS and DBCS obtained from the maxima and minima of the transmission coefficient, respectively. (b) Transmission spectra for some values of δ. Red and blue curves give the theoretical transmission without and with loss, respectively, while green open circles give the experimental measurements. The arrows indicate the frequencies of the transmission minima associated to two DBCS modes. (c) Variation of the theoretical transmission (in color scale) as a function of Ω and δ for $d_1 = 1$. Cyan circle indicates the FW BIC position. (d) Exact (solid line) and approximate (open circles) results of the EIT resonance for $d_1 = 1$ and $\delta = 0.1$.

Similarly, Eq. (4) giving the NBCS modes can also be factorized by $S = 0$ (since $S_1 = S$) and therefore $kd = \pi$ (or $\Omega = 1$) is a solution of $\rho = 0$ whatever the value of δ.

These analytical results are confirmed in Fig. 3(a) displaying the dispersion curves of NBCS (pink curves) and DBCS (cyan curves) as a function of δ for $d_1 = 1$. One can notice a horizontal branch associated to NBCS at $\Omega = 1$, which remains constant whatever the value of δ. Also, two branches of DBCS cross each other at $\Omega = 1$ and $\delta = 0$ with no coupling strength $\kappa = 0$. By slightly shifting from $\delta = 0$, one can notice a lifting of degeneracy between the two DBCS branches, the separation between them depends on δ following Eq. (15). The intersection of DBCS and NBCS branches gives rise to a FW BIC without coupling at $\Omega = 1$ and $\delta = 0$. For $\delta \neq 0$, the FW BIC transforms to a resonance (i.e., $\rho = 0$, pink branch) squeezed between two transmission zeros (i.e., $\tau = 0$, cyan branches). The FW BIC behavior is also obtained in the transmission spectra as shown in Fig. 3(b). The FW BIC occurs at the crossing of two transmission zeros (indicated by vertical arrows) at $\Omega = 1$ for $\delta = 0$. By increasing δ, a transparency window appears between two transmission dips giving rise to a symmetric EIT resonance as shown for $\delta = 0.1$ and $\delta = 0.3$. The separation between the two transmission dips increases as δ increases according to Eq. (15), giving rise to an EIT resonance for $\delta < 0.3$ and ATS resonance for $\delta > 0.5$. The distinction between EIT and ATS resonances using an AIC test is discussed in the Supplemental Material SM4 [76]. The evolution of the transmission coefficient as a function of δ and Ω is shown in color scale in Fig. 3(c).

The FW BIC is indicated by a cyan circle at $\delta = 0$ and $\Omega = 1$. By shifting from $\delta = 0$, the BIC transforms to a resonance squeezed between two transmission dips.

In order to confirm that the transmission resonance in Fig. 3(c) for δ close to zero is of EIT type, we have performed an approximate expression of the transmission rate in the vicinity of the resonance frequency. A Taylor expansion of the transmission coefficient at $d_1 = 1$ and around $\Omega = 1 + \varepsilon$ (with $\varepsilon << 1$) enables us to rewrite the transmission rate as

$$T = A \frac{(\varepsilon - q_1 \Gamma)^2 (\varepsilon - q_2 \Gamma)^2}{\varepsilon(\varepsilon + \beta) + \Gamma^2}, \qquad (16)$$

where $A = 4/\alpha$, $\alpha = 16\Delta'^4/\pi^2 - 7\Delta'^2 + 1$, and $\beta = 16\Delta'^4/\pi\alpha$ with $\Delta' = \pi\delta/2d$. The FWHM of the EIT resonance at $\varepsilon = 0$ (i.e., $\Omega = 1$) is given by $\Gamma = 2\Delta'^2/\sqrt{\alpha}$. $q_1 = \sqrt{\alpha}/2\left[1/\pi - 1/\Delta'\pi\sqrt{\Delta'^2 + \pi^2}\right]$, and $q_2 = \sqrt{\alpha}/2\left[1/\pi + 1/\Delta'\pi\sqrt{\Delta'^2 + \pi^2}\right]$ are the coupling (or Fano [24]) parameters that describe the strength of the interference between the bound state and the propagating continuum of states. Equation (16) shows that the EIT resonance appears as a Lorentzian at $\varepsilon = 0$ squeezed between two transmission zeros at $\varepsilon_1 = q_1 \Gamma$ and $\varepsilon_2 = q_2 \Gamma$. The separation between the two zeros is given by

$$\Delta\varepsilon = (q_1 - q_2)\Gamma = \frac{2\Delta'}{\pi}\sqrt{\Delta'^2 + \pi^2}. \qquad (17)$$

An example of the approximate result of the transmission [Eq. (16)] is given by open circles in Fig. 3(d) in comparison with the exact results (blue curve) for $d_1 = 1$ and $\delta = 0.1$. The approximate results fit well the exact ones and show that the resonance is an EIT-like resonance with $q_1 = -2.76$, $q_2 = 3.04$, and $\Gamma = 0.044$.

3. Approximate results around the two interacting modes

A Taylor expansion of Eq. (11) around $d_1 = 1$ (i.e., $d_1 = 1 + \Delta$ with $\Delta << 1$) and $\Omega = 1$ (i.e., $\Omega = 1 + \varepsilon$ with $\varepsilon << 1$) enables us to get an approximate expression of the coupling strength κ. This quantity is defined as the distance between two DBCS modes, namely (see the Supplemental Material SM5 [76])

$$\kappa = |\Omega_2 - \Omega_1| = \left|\frac{\Delta}{\Delta + \pi}\right|. \qquad (18)$$

Equation (18) shows that when $\Delta = 0$ (i.e., $d_1 = 1$), the coupling strength κ vanishes, which means that there is no coupling between the two DBCS branches. While for $\Delta \neq 0$, we can distinguish between two regions of strong and weak coupling depending on the value of Δ (i.e., d_1).

Figures 4(a)–4(e) show a comparison between exact (cyan circles) and approximate (red triangles) eigenmodes

of DBCS around $\Omega = 1$ and for some values of d_1 around $d_1 = 1$, such as $d_1 = 0.8$ [Fig. 4(a)], $d_1 = 0.9$ [Fig. 4(b)], $d_1 = 1$ [Fig. 4(c)], $d_1 = 1.1$ [Fig. 4(d)], and $d_1 = 1.2$ [Fig. 4(e)]. The approximate results reproduce well the exact results. One can see the existence of a FW BIC at the crossing of one DBCS branch and one NBCS branch at $\Omega = 1$ and $\delta = 0$. Another DBCS branch appears at $\Omega > 1$ for $d_1 < 1$ [Figs. 4(a) and 4(b)], crosses the first one at $d_1 = 1$ and $\Omega = 1$ [Fig. 4(c)] and reappears at $\Omega < 1$ for $d_1 > 1$ [Figs. 4(d) and 4(e)]. Figure 4(f) shows the coupling strength κ between the two DBCS branches as a function of d_1 around $d_1 = 1$. It can be seen that κ depends strongly on d_1. For $d_1 = 1$, the two DBCS branches cross each other with no coupling between them ($\kappa = 0$). For $d_1 \neq 1$, κ is different from zero and one can distinguish between two regions of strong and weak coupling depending on the value of d_1 (see below). Red triangles in Fig. 4(f) give the results obtained from the approximate expression in Eq. (18). This result reproduces well the exact result around $d_1 = 1$. Open circles show the experimental measurements deduced from Fig. 5(a). In order to quantify the coupling strength, we have presented in Fig. 4(g) κ and the sum of the linewidths of the modes $\gamma_+ + \gamma_-$ for d_1 around an integer value ($d_1 = 1$). For the two resonances to be spectrally separable, the minimum mode splitting needs to be greater than the sum of the linewidths of the modes, which is a necessary condition to observe strong coupling, otherwise it is considered as a weak coupling [3,20]. From Fig. 4(g), one can distinguish the regions of d_1 with strong and weak coupling. The coupling is weak for $0.71 \leq d_1 \leq 1.3$, and becomes strong for $d_1 < 0.71$ and $d_1 > 1.3$. These results show that the two cases discussed before ($d_1 = 1$ and $d_1 = 0.8$) correspond to weak coupling regime. In addition, similar results can be obtained for two modes of NBCS around a half-integer value of d_1 ($d_1 = 0.5$) where another coupling strength κ' can be noticed between two NBCS branches (see Fig. S6 within the Supplemental Material SM7 [76]).

B. Effect of the vertical stub of length d_1

In this subsection, we will discuss the effect of the length d_1 of the vertical stub on the BICs and the induced resonances EIT and EIR. As mentioned before, the BICs are obtained when d_2 and d_3 are chosen commensurate. Here, we focus on the BICs given by $d_2 = d_3$ (i.e., $\delta = 0$). For this purpose, Eqs. (3) and (4) can be rewritten as a function of δ as follows:

$$\tau = 2C_3(C_1 C_2 - 2S_1 S_2) + 2S_1 \sin(k\delta), \qquad (19)$$

and

$$\rho = C_2(S_1 C_3 + 2C_1 S_3) + C_1 \sin(k\delta). \qquad (20)$$

For $\delta = 0$ (i.e., $d_2 = d_3$ and $C_2 = C_3$), the second term at the right-hand side of Eq. (19) vanishes giving rise to a
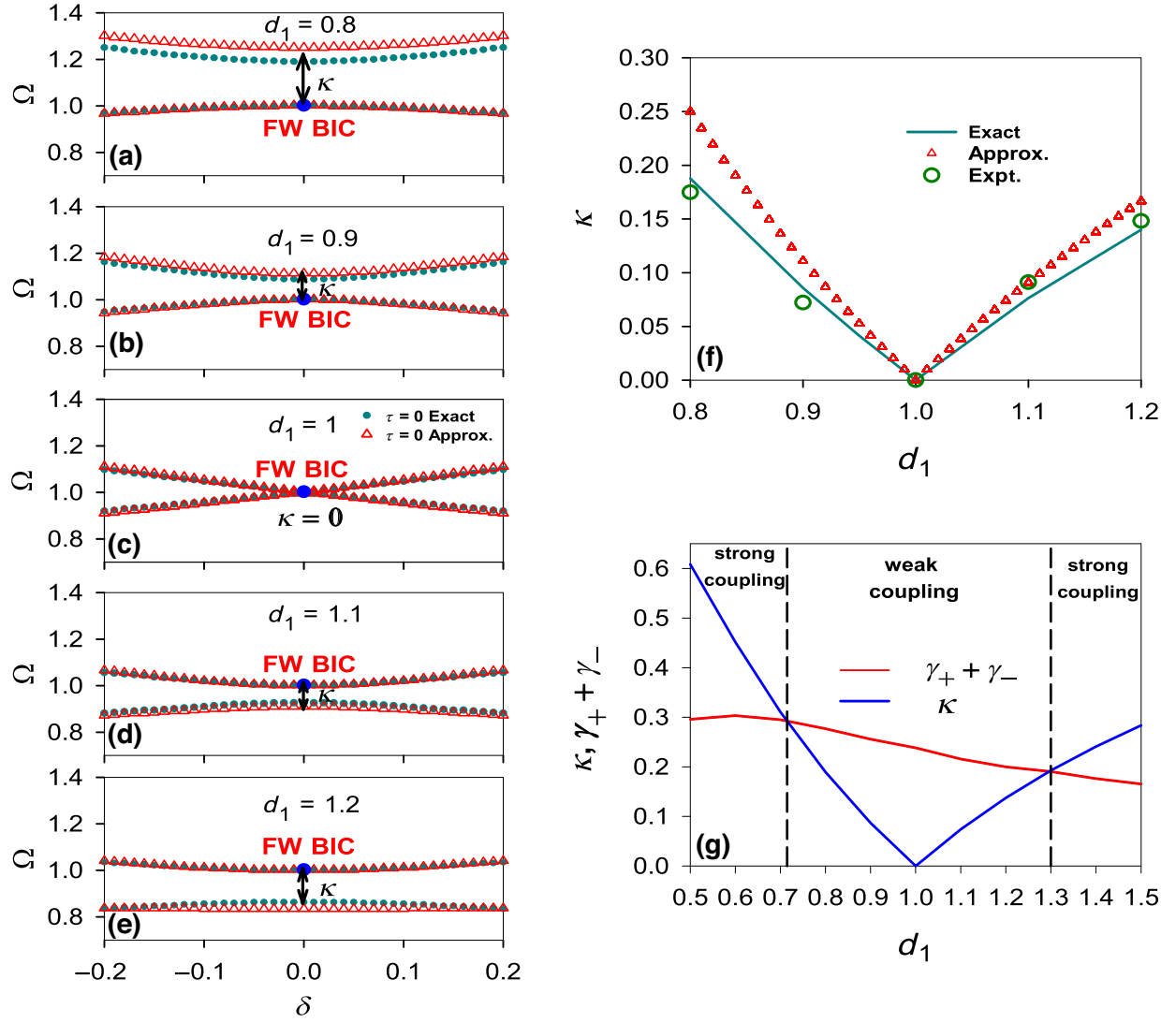
FIG. 4. (a)–(e) Exact (cyan circles) and approximate (red triangles) eigenmodes of DBCS around $\Omega = 1$ and for some values of d_1 around $d_1 = 1$, such as $d_1 = 0.8$ (a), $d_1 = 0.9$ (b), $d_1 = 1$ (c), $d_1 = 1.1$ (d), and $d_1 = 1.2$ (e). The blue circle indicates the FW BIC position. (f) The coupling strength κ (cyan curve) between the two branches in (a)–(e) as a function of d_1. The red triangles show the approximate results of κ [Eq. (18)] around $d_1 = 1$, while open circles give the experimental measurements. (g) Dependence of κ and sum of linewidths $\gamma_+ + \gamma_-$ on d_1.

decoupling of two modes of DBCS, namely

$$C_2 = 0, \tag{21}$$

and

$$C_1 C_2 - 2 S_1 S_2 = 0. \tag{22}$$

In the same way, the modes of NBCS in Eq. (20) can be also factorized into two decoupled modes,

$$C_2 = 0, \tag{23}$$

and

$$S_1 C_2 + 2 C_1 S_2 = 0. \tag{24}$$

Equations (21) and (23) show that $C_2 = 0$ are common modes of DBCS and NBCS. Therefore, these modes represent BICs, which are independent of d_1. These BICs are given by $kd_2 = k(d)/2 = (2n+1)\pi/2$ (where n is an integer) or equivalently

$$\Omega = 2n + 1. \tag{25}$$

At the BIC frequency [Eq. (25)], the transmission rate becomes simply

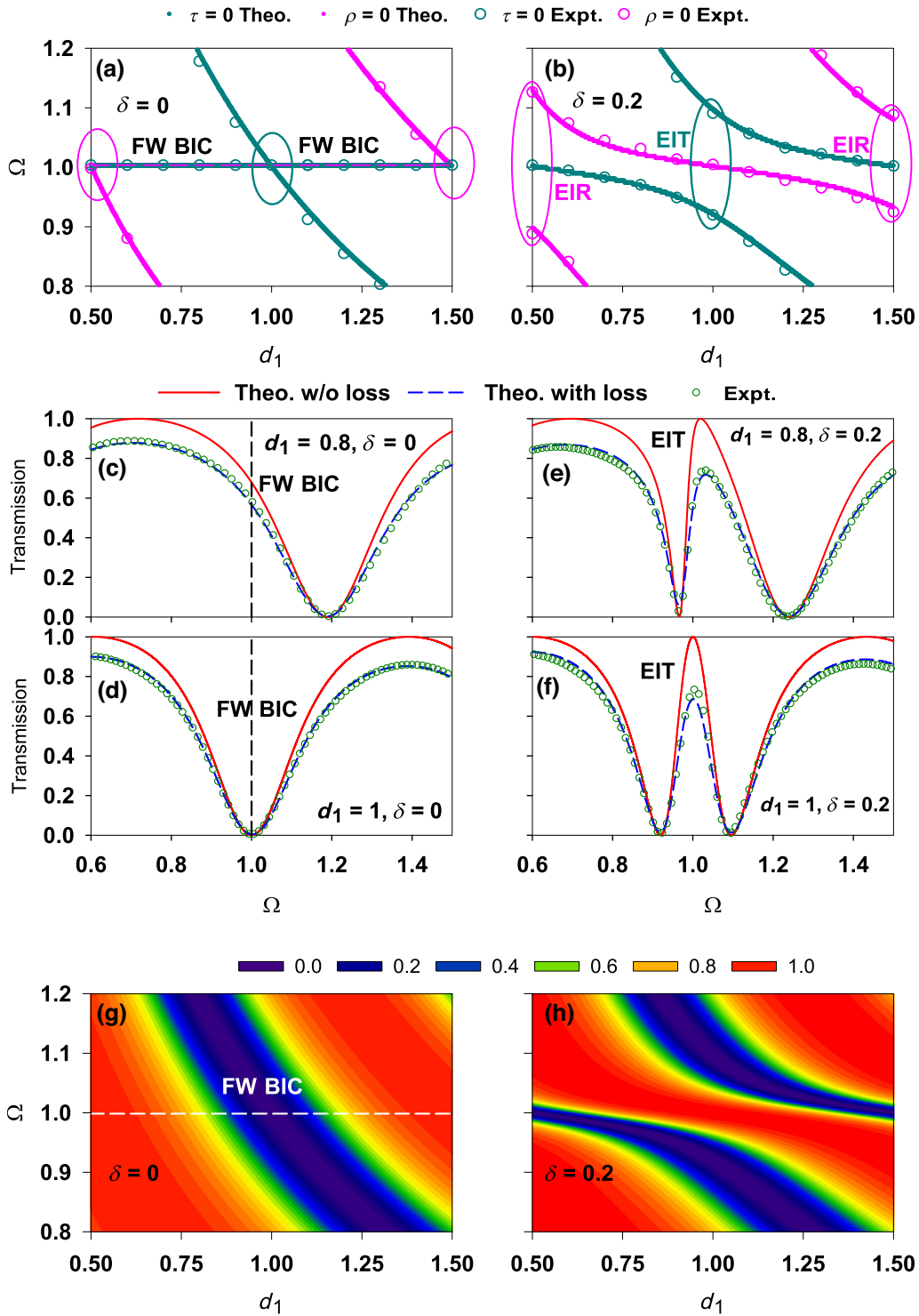$$T = \frac{4 S_1^2}{4 S_1^2 + C_1^2}. \tag{26}$$

FIG. 5. (a),(b) Dispersion curves of the system depicted in Fig. 1 with NBCS ($\rho = 0$, pink curves) and DBCS ($\tau = 0$, cyan curves) as a function of d_1 for $\delta = 0$ and $\delta = 0.2$, respectively. Pink and cyan circles give the experimental eigenmodes for NBCS and DBCS obtained from the maxima and minima of the transmission coefficient, respectively. The large circles in (a) indicate the position of BICs, while in (b) they indicate the position of EIT and EIR resonances depending on the value of d_1. (c),(d) Transmission spectra in the case $\delta = 0$ for $d_1 = 0.8$ and $d_1 = 1$, respectively. (e),(f) Transmission spectra in the case $\delta = 0.2$ for $d_1 = 0.8$ and $d_1 = 1$, respectively. Red and blue curves represent the theoretical transmission without and with loss, respectively, while green open circles give the experimental measurements. (g),(h) Theoretical transmission spectra (in color scale) as a function of Ω and d_1 for $\delta = 0$ and $\delta = 0.2$, respectively. The horizontal dashed line at $\Omega = 1$ in (g) indicates the position of the robust BIC as a function of d_1.

Also, from Eqs. (21) and (22) one can deduce that two modes of DBCS cross each other for $C_2 = 0$ [i.e., $kd_2 = k(d)/2 = (2n+1)\pi/2$] and $S_1 = 0$ ($kd_1 = m_1\pi$) where m_1 is an integer. Therefore, we get

$$\frac{d_1}{d} = \frac{m_1}{2n+1}. \tag{27}$$

Similarly, Eqs. (23) and (24) show that the NBCS modes cross each other for $C_2 = 0$ [i.e., $kd_2 = k(d)/2 = (2n+1)\pi/2$] and $C_1 = 0$ [i.e., $kd_1 = (2m_1+1)\pi/2$], namely

$$\frac{d_1}{d} = \frac{(2m_1+1)}{2(2n+1)}. \tag{28}$$

In order to give a numerical and experimental validation of all these analytical results, we provide in Figs. 5(a) and 5(b) the dispersion curves of NBCS ($\rho = 0$, pink curves) and DBCS ($\tau = 0$, cyan curves) as a function of d_1 for $\delta = 0$ and $\delta = 0.2$, respectively. The results are given around the first mode ($n = 0$, $\Omega = 1$). For $\delta = 0$ [Fig. 5(a)], one can notice the existence of a common mode of DBCS and NBCS at $\Omega = 1$. This mode represents a robust BIC, which remains pinned at $\Omega = 1$ whatever the value of d_1. The DBCS modes (cyan curves) cross each other at $\Omega = 1$ and $d_1 = 0, 1$ [i.e., $m_1 = 0, 1$ in Eq. (27)], while the NBCS modes (pink curves) intersect at $d_1 = 0.5, 1.5$ [i.e., $m_1 = 0, 1$ in Eq. (28)] giving rise to two degenerate modes. For $\delta = 0.2$ [Fig. 5(b)], one can notice a lifting of degeneracy of the modes giving rise to either a transmission zero between two transmission maxima (EIR resonance) around $d_1 = 0.5$ and $d_1 = 1.5$ or a transmission maximum between two transmission zeros (EIT resonance) around $d_1 = 0$ (not shown here) and $d_1 = 1$. The experimental eigenmodes of DBCS and NBCS (open circles) are obtained, respectively, from the minima and maxima of the experimental transmission spectra [Figs. 5(c)–5(f)]; these data reproduce very well the theoretical dispersion curves.

We will focus on the EIT resonance indicated by a large cyan circle in Fig. 5(b) around $d_1 = 1$. The behavior of the EIR resonances falling around $d_1 = 0.5$ and $d_1 = 1.5$ (indicated by large pink circles) is discussed in the Supplemental Material SM3 [76]. Figures 5(c) and 5(d) show two examples of transmission spectra in the case $\delta = 0$ with $d_1 = 0.8$ and $d_1 = 1$, respectively. Red and blue curves represent the theoretical transmission without and with loss, respectively, while green open circles give the experimental measurements. The BIC does not show any signature in the transmission spectra and appears as a zero-width resonance, but with an amplitude $T \simeq 0.68$ for $d_1 = 0.8$ [Fig. 5(c)] and as a transmission zero for $d_1 = 1$ [Fig. 5(d)] in accordance with Eq. (26). For $\delta = 0.2$, we give in Figs. 5(e) and 5(f) two examples of transmission spectra for $d_1 = 0.8$ and $d_1 = 1$, respectively. One obtains

an EIT resonance placed either asymmetrically or symmetrically between two transmission zeros depending on the value of d_1. For $d_1 = 1$, the coupling strength between DBCS branches is given by Eq. (17). In the presence of loss, the amplitude of the transmission is considerably affected and does not reach unity (blue dashed lines and green open circles), however the behavior and the width of the EIT resonances still remain unaffected. These results are better explained in color scale in the transmission spectra where we have plotted in Figs. 5(g) and 5(h) the theoretical transmission as a function of Ω and d_1 for $\delta = 0$ and $\delta = 0.2$, respectively. For $\delta = 0$ [Fig. 5(g)], the BIC remains robust at $\Omega = 1$ (horizontal dashed line) as a function of d_1. At $\Omega = 1$, the transmission decreases form one at $d_1 = 0.5$ to zero at $d_1 = 1$ and back to one at $d_1 = 1.5$ in accordance with Eq. (26). For $\delta = 0.2$ [Fig. 5(h)], the BIC transforms into an EIT around $d_1 = 1$ or EIR resonance around $d_1 = 0.5$ and 1.5.

In addition to the transmission and reflection coefficients, another interesting quantity used to determine the distribution and the weight of the modes of the system is the variation of the DOS. The Green's function approach enables us to determine the variation of the DOS of the system depicted in Fig. 1(a) and a reference system made of decoupled waveguides. Also, for a lossless system, the variation of the DOS is related to the phase of the determinant of the scattering matrix S (i.e., the so-called Friedel phase θ_F [66]), which can be measured experimentally [78]. Their relationship is the following:

$$\frac{d}{d\omega}\text{Arg}[\det(S)] = \frac{d\theta_F}{d\omega} = 2\pi\,\Delta n(\omega). \tag{29}$$

Equation (29) still remains valid for low-loss systems, which can be used to derive the DOS from the measurement of the Friedel phase. A numerical and experimental validation of the latter relation is given in the Supplemental Material SM6 [76].

IV. APPLICATION TO PLASMONIC WAVEGUIDES: NUMERICAL EVIDENCE IN THE INFRARED DOMAIN

A. Transposition to nanometric *M-I-M* waveguides

The previous analytical results presented in Sec. II can be also transposed to a T-shaped plasmonic device based on *M-I-M* waveguides operating in the infrared domain [Fig. 1(c)]. The proposed platform is a two-dimensional (2D) plasmonic model made up of an infinite *M-I-M* waveguide and a side-coupled T-shaped cavity, assuming that the medium of the waveguide and the T-shaped cavity are filled with air ($\varepsilon_d = 1$), while the surrounding metal is made of silver (Ag) with a dielectric constant ε_m described

by the Drude model [79–82]

$$\varepsilon_m = \varepsilon_\infty - \frac{\omega_p^2}{\omega^2 + j\gamma\omega}, \tag{30}$$

where $\varepsilon_\infty = 3.7$ is the dielectric constant at an infinite frequency, $\omega_p = 1.38 \times 10^{16}$ rad/s is the bulk plasma frequency of free conduction electrons, $\gamma = 2.634 \times 10^{13}$ rad/s is the electron collision frequency, and ω is the angular frequency of the incident wave. These parameters fit well the experimental results in the visible and infrared frequency domains [43]. In these regimes, Ag has been widely used in *M-I-M* plasmonic waveguides because of its low absorption and power consumption in comparison with other plasmonic metals [42,43]. However, our model can also be transposed to other metals of practical use in plasmonics such as gold (Au), aluminium (Al), etc. Here, the width of the bus waveguide and the T-shaped cavity is fixed to $w = 50$ nm in order to ensure only the propagation of the fundamental transverse magnetic (TM_0) mode excitation. The structure depicted in Fig. 1(c) is a 2D system in the (x,y) plane and infinite in the z direction. This design is the most used in *M-I-M* waveguide simulations as it is less time consuming than 3D simulations. However, for practical processing, the *M-I-M* waveguides are 3D as they present a finite height h along the z direction and they are deposited on SiO$_2$ substrate. The finite depth of the system and the surrounding media introduce a significant effect on loss in the system. Nevertheless, it was shown that above a certain height ($h = 50$ nm), 2D and 3D models provide almost similar results [83,84], in particular, as concerns the positions of the resonant modes in the transmission spectra despite the fact that their shapes and widths can be affected by the loss of the metal [83,84]. In addition, it was shown that 2D *M-I-M* waveguides can be handled analytically using an equivalent 1D system where a surface plasmon polariton wave vector k_{sp} is introduced [80,81,85]. The advantage of the 1D model lies in the derivation of the analytical expressions of the dispersion relations, DOS, and transmission and reflection coefficients in closed form, which enables the origin of the different modes propagating in such systems to be understood deeply. In order to operate in the infrared domain, the structural parameters of the T-shaped cavity are set to be $d = d_2 + d_3 = 550$ nm and $d_1 = d$ and the detuning δ between the two stubs d_2 and d_3 is chosen variable.

The calculation of the transmission coefficient and the dispersion relation are similar to those presented in the previous section (Sec. II A), provided we permute k by k_{sp} given by

$$k_{sp} = k_0 \sqrt{\varepsilon_d - \frac{2\varepsilon_d\sqrt{\varepsilon_d - \varepsilon_m}}{\varepsilon_m k_0 w}} \tag{31}$$

and F by ωZ where the impedance Z is given by

$$Z = \frac{k_{sp}w}{\varepsilon_d\omega}. \tag{32}$$

Here ε_d and ε_m are the dielectric constants of the dielectric and metal, respectively. $k_0 = \omega/c$ is the wave vector in vacuum and c is the speed of light in vacuum. The details of calculation of these two physical quantities are given in Ref. [85].

Similarly to the photonic case (Sec. III), we present in Figs. 6(a) and 6(b), respectively, the analytical and numerical results of the transmission amplitude (in color scale) as a function of the wavelength and the detuning $\delta = d_2 - d_3$ and for fixed $d_1 = d = d_2 + d_3 = 550$ nm in the case of no coupling regime $\kappa = 0$. The value of d is chosen such that the BIC and the corresponding PIT resonances fall around the telecom wavelength ($\lambda = 1550$ nm). The analytical results are obtained by means of the Green's function method [Fig. 6(a)], whereas the numerical results are performed by using COMSOL Multiphysics software based on the 2D finite-element method [Fig. 6(b)]. Both results show a good agreement. One can see that a FW BIC appears at $\lambda = 1556$ nm for $\delta = 0$. By increasing δ, the BIC transforms to a PIT resonance for $\delta < 100$ nm and ATS resonance for $\delta > 100$ nm. One can notice that the transmission does not reach unity ($T_{\max} = 0.8$) because of the losses in the metal. We give in Fig. 6(c) some transmission spectra for different values of δ. The blue solid lines represent the analytical results, while open circles show the numerical results. As predicted, a FW BIC can be seen around $\lambda = 1556$ nm, indicated by the black arrow for $\delta = 0$. When we shift away from the BIC condition, the BIC transforms into a well-defined PIT resonance for $\delta < 100$ nm and ATS resonance for $\delta > 100$ nm. The intensity and width of the resonance increase as δ increases as shown in Fig. 6(c). As δ increases, a transition from PIT to ATS occurs around $\delta = 100$ nm. Then, an ATS resonance is obtained for $\delta = 150$ and $\delta = 200$ nm where the transparency window becomes broader.

In order to show the magnetic field localization (H_z-field map) of the BIC and PIT resonance in Fig. 6(c), we have applied a local magnetic excitation at the boundary of the guide d_2 (indicated by a red arrow). Figure 6(d) shows the H_z-field map of the BIC mode at $\lambda = 1556$ nm for $\delta = 0$ (i.e., $d_2 = d_3$) in Fig. 6(c). As expected for a BIC, the mode remains well confined within the two horizontal guides without radiating into the rest of the system. The magnetic field vanishes at the midpoint of the two guides d_2 and d_3 where they intersect with the vertical stub d_1. It has an antisymmetric shape with respect to the middle of the segment. This behavior can be also proved analytically from the definition of the BIC in Eq. (8). Similarly, Fig. 6(e) shows the H_z-field map for the filtered PIT resonance at $\lambda = 1556$ nm for $\delta = 80$ nm in Fig. 6(c). Here, we deviate
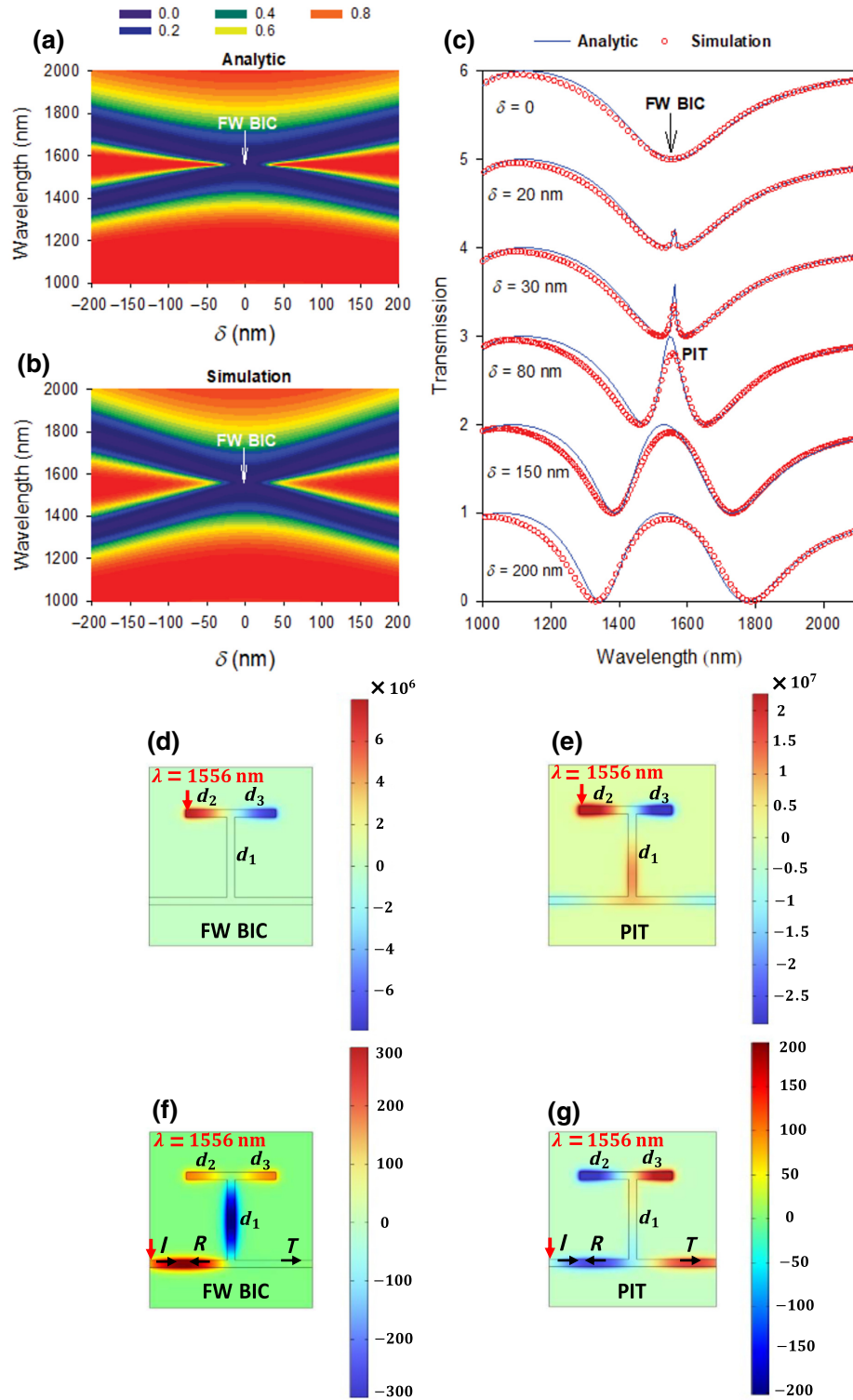
FIG. 6. (a),(b) Analytical and numerical variation of the transmission coefficient (in color scale) as a function of the wavelength and the detuning $\delta = d_2 - d_3$ and for fixed $d_1 = d = d_2 + d_3 = 550$ nm, respectively. The arrows in (a),(b) indicate the position of the FW BIC. (c) Transmission coefficient versus the wavelength for various values of the detuning δ and for fixed $d_1 = 550$ nm. Blue and red curve correspond to analytical and numerical results, respectively. The black arrow in (c) indicates the position of the FW BIC. (d) H_z-field map of the BIC at $\lambda = 1556$ nm for $\delta = 0$ in (c) when a local magnetic excitation is applied at the boundary of the guide d_2. (e) Same as in (d) but for the PIT resonance at $\lambda = 1556$ nm for $\delta = 80$ nm in (c). (f),(g) H_z-field maps of the BIC and the filtered PIT resonance excited by an incident wave in the left semi-infinite waveguide. I, R, and T denote the incident, reflected, and transmitted waves, respectively. The red arrow in (d)–(g) indicates the position of the excitation.

from the condition of a perfect BIC, which transforms into a quasi-BIC. For this reason, the eigenmode displays some leakage into the rest of the structure while the field remains stronger in the horizontal guides.

Another way to study the coupling of the T structure with the infinite guide consists of sending an incident wave from the left semi-infinite waveguide (indicated by a red arrow) and calculate the reflected and transmitted waves. Figures 6(f) and 6(g) show the results for the BIC and PIT resonance, respectively. The field map in Fig. 6(f) shows a degenerate mode of the whole cavity with the BIC mode with vanishing magnetic field at all the connection points. This mode is totally reflected as it coincides with a transmission zero. For the filtered PIT resonance [Fig. 6(g)], the mode of the whole horizontal guide of length $d_2 + d_3$ is excited and spread throughout the whole cavity. This mode is totally transmitted as the stub d_1 is connected far from the point where the magnetic field vanishes in the horizontal guide, giving rise to a full transmission. These results show the possibility to use the T cavity as

selective or rejective filters for given wavelengths depending on the geometrical parameters. Let us mention that for a 3D realistic model, the presented results will be quantitatively different from those obtained with a 2D model based on finite element method and a 1D model based on Green's function. However, the general trends will remain the same as concerns the observation of the PIT resonances as it was demonstrated in recent experimental realizations [51–53] (see the Supplemental Material SM8 and Fig. S7 [76]).

B. Structural sensing application

The BIC and resonance frequencies of the *M-I-M* plasmonic waveguide are sensitive to the properties of the dielectric that fills the space between the metals. Taking advantage of their high-Q factors, Fano and PIT resonances are widely used for refractive-index sensing and biosensing applications [42–49]. In what follows, we show the ability of our plasmonic device for both applications.
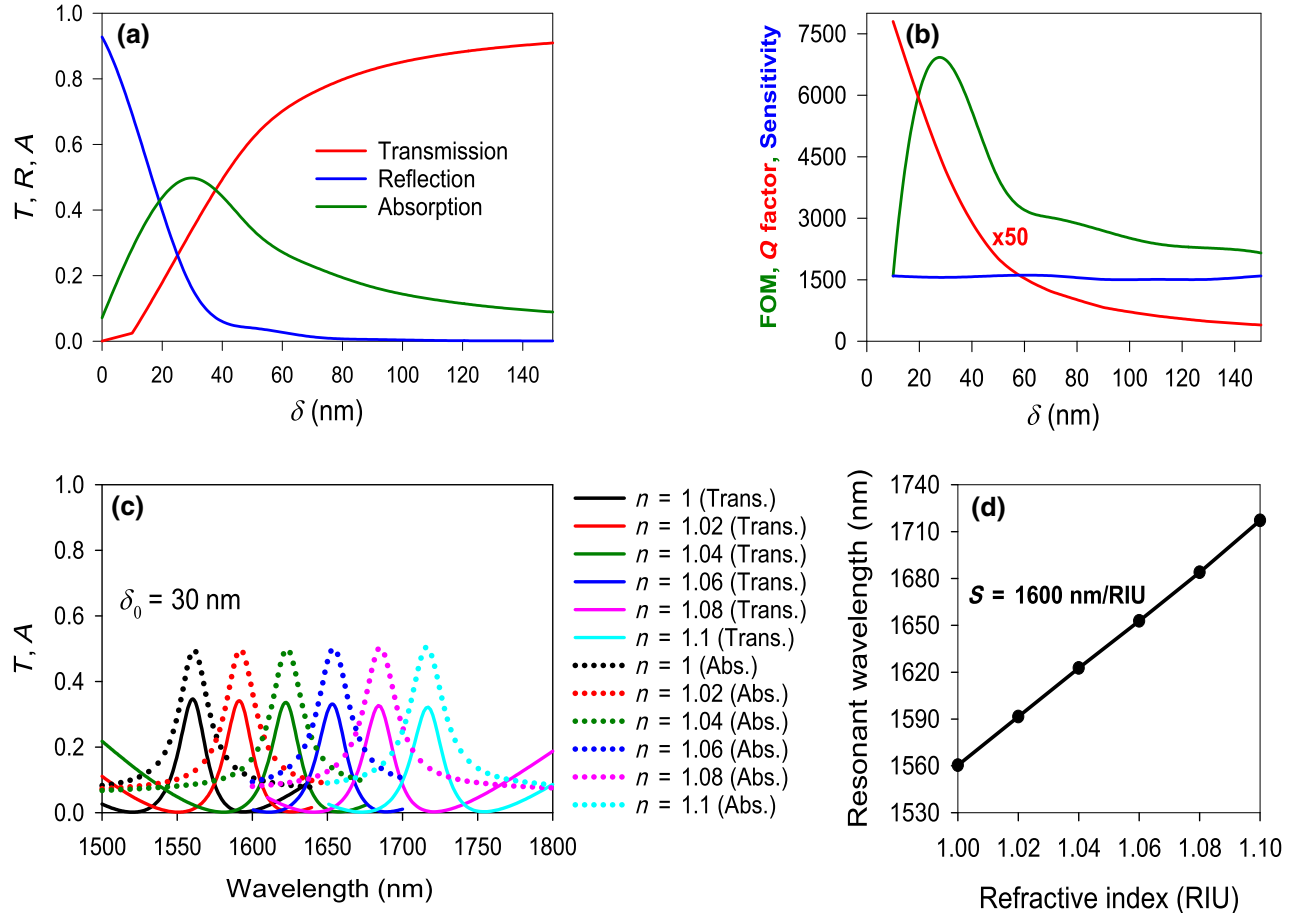

FIG. 7. (a) Numerical variation of the transmission (red line), reflection (blue line) and absorption (green line) as a function of the detuning $\delta = d_2 - d_3$ at the PIT resonant wavelength $\lambda = 1556$ nm in Fig. 6(c). (b) FOM (green), quality factor (red) and sensitivity (blue) as a function of δ. The values of quality factor are multiplied by a factor of 50 to be on the same scale with the sensitivity and FOM. (c) Transmission (continuous lines) and absorption (dotted lines) spectra versus the wavelength for different refractive index n in the waveguide. (d) The evolution of resonant wavelength as a function of the refractive index n.

1. Gas sensing

The performance of a sensor is essentially highlighted by its sensitivity (S) to material changes and its figure of merit (FOM). The sensitivity of a refractive-index sensor is determined by the shift of the resonance wavelength $\Delta\lambda$ due to refractive index changes Δn, and is defined as [86]

$$S = \frac{\Delta\lambda}{\Delta n}. \tag{33}$$

Also, FOM at a fixed wavelength is defined as [86]

$$\text{FOM} = \left[\frac{\Delta T}{T\Delta n}\right]_{\max}, \tag{34}$$

where T and ΔT denote, respectively, the amplitude of the transmission and its variation due to the change Δn in the refractive index.

The PIT resonance falling at $\lambda = 1556$ nm can be used to study the sensitivity and FOM of our device. However, these two quantities depend on the detuning δ. Indeed, based on the simulations results, the transmission, reflection, and absorption at the PIT resonance, depend strongly on δ as shown in Fig. 7(a). When δ increases, the transmission T increases, the reflection R decreases, while the absorption A goes through a maximum value ($A \simeq 0.5$) when $T = R \simeq 0.25$ at a given value of $\delta_0 = 30$ nm. Figure 7(b) shows FOM (green), quality factor (red), and sensitivity (blue) as a function of δ. The values of quality factor are multiplied by a factor of 50 to be on the same scale with the sensitivity and FOM. The FOM shows a maximum value at $\delta_0 = 30$ nm, whereas the sensitivity remains almost constant as a function of δ. In contrast, the quality factor Q, which reaches 83 at δ_0 can become larger for lower values of δ ($\delta < \delta_0$) as illustrated in Fig. 7(b). However, for $\delta < \delta_0$, the amplitude of the resonances in the transmission spectra becomes very small [see Fig. 6(c)]. Particularly, for δ close to zero, the width of the resonance in the transmission becomes ill defined [Fig. 6(c)] and so the Q factor, due to very low amplitude of the resonance. These results show that the best value of δ to get a resonance with a large value of FOM, the best quality factor without the distortion of the transmission resonance can be obtained for δ close to δ_0. An example of the calculation of the sensitivity for $\delta_0 = 30$ nm and $d_1 = d = 550$ nm is given in Figs. 7(c) and 7(d). Figure 7(c) shows the transmission (continuous lines) for different values of the refractive index n of the dielectric in the waveguides, which ranging from $n = 1$ to $n = 1.1$ with a step of 0.02. The PIT resonance in the transmission spectra shifts linearly towards high wavelengths as n increases. Dotted lines in Fig. 7(c) represent the absorption in the system as a function of the wavelength for different values of n. Figure 7(d) shows the evolution of the transmission resonant wavelength in Fig. 7(c) as a function of the refractive index n.

From the slope of this graph, one can deduce a maximum sensitivity of 1600 nm/RIU and a FOM of 0.7×10^4 at $\lambda = 1594.1$ nm.

Table I gives a comparison of our results of the sensitivity and FOM with those of previous similar refractive-index sensors based on M-I-M waveguides coupled to stubs. Most refractive-index plasmonic sensors are based on Fano resonances as the latter show a better performance in terms of sensitivity and FOM in comparison with other types of resonances like EIT [42,43]. In comparison with other similar refractive-index sensors, our design shows a good sensitivity and a comparable value of FOM. For the sake of comparison with other plasmonic refractive-index sensors, we have used silver as metal, but our approach remains valid and can be used for either silver or gold plasmonic waveguides (see Fig. S7 in the Supplemental Material SM8 [76]).

2. Biosensing

The proposed M-I-M plasmonic device is also suitable for use as a nanoscale biosensor, for instance, to measure the concentration of different analytes, such as unknown samples from a specific blood group. The design can be easily miniaturized and provides a label-free detection and low cost [31,44,46,48,67]. Here, we propose our system to detect specific electrolytes (Na^+ and K^+) and glucose concentrations from human blood samples. All the remaining geometrical parameters of the biosensor are the same as those used in the previous section (Sec. IV B 1). It is well known from the literature that there is a relationship between the concentration of the sample and the refractive index [87,88], namely

$$n_{Na^+} = 1.3373 + 1.768 \times 10^{-3}\left(\frac{Ck}{393}\right)$$
$$- 5.8 \times 10^{-6}\left(\frac{Ck}{393}\right)^2, \tag{35}$$

TABLE I. Comparison of the sensitivity and FOM with recently reported refractive-index sensors.

Structure design	Sensitivity (nm/RIU)	FOM	Resonance
Ref. [70]	1100	2×10^5	Fano
Ref. [71]	530	650	Fano
Ref. [72]	1200	———	PIT
Ref. [73]	820	3.2×10^5	Fano
Ref. [74]	1060	176.7*	Fano
Ref. [60]	680	———	Fano
Our design	1600	0.7×10^4	PIT

* This value is calculated from the expression FOM $= S/$FWHM instead of Eq. (34).

$$n_{K^+} = 1.3353 + 1.6167 \times 10^{-3} \left(\frac{Ck}{529.8} \right)$$

$$- 4 \times 10^{-7} \left(\frac{Ck}{529.8} \right)^2, \tag{36}$$

$$n_{\text{glucose}} = 0.00011889Ck + 1.33230545, \tag{37}$$

where C indicates the concentration in mg/dl, and k is the concentration factor: $k = 30, 50,$ and 10 for Na^+, K^+ and glucose solution, respectively.

The performance of a biosensor is characterized by its sensitivity (S') to concentration changes, which is defined as $S' = \Delta\lambda/\Delta C$. In order to evaluate the performance of our plasmonic biosensor, the medium of the bus waveguide and the T-shaped cavity are filled with different concentrations of Na^+ and K^+ and glucose solution. The

concentrations of Na^+, K^+ and glucose solutions were, respectively, set from 200 to 440 mg/dl with an interval of 60 mg/dl, from 0 to 80 mg/dl with an interval of 20 mg/dl and from 110 to 230 mg/dl with an interval of 30 mg/dl. Their transmittance curves are presented in Figs. 8(a)–8(c) revealing a distinguishable transmission peak shifts as the concentrations are varied, with an increase of the resonance wavelengths with the concentrations. The frequency shifts exhibit a linear behavior shown in the insets of Figs. 8(a)–8(c). From the slopes of these plots one can deduce a maximum sensitivity of 0.17, 0.23, and 1.84 nm dl/mg for Na^+, K^+ and glucose solutions, respectively. These results are comparable to those of other plasmonic biosensors in the literature within the range of 1800–2600 nm [48,67–69]. Based on this comparative study, the proposed biosensor has the advantage of being
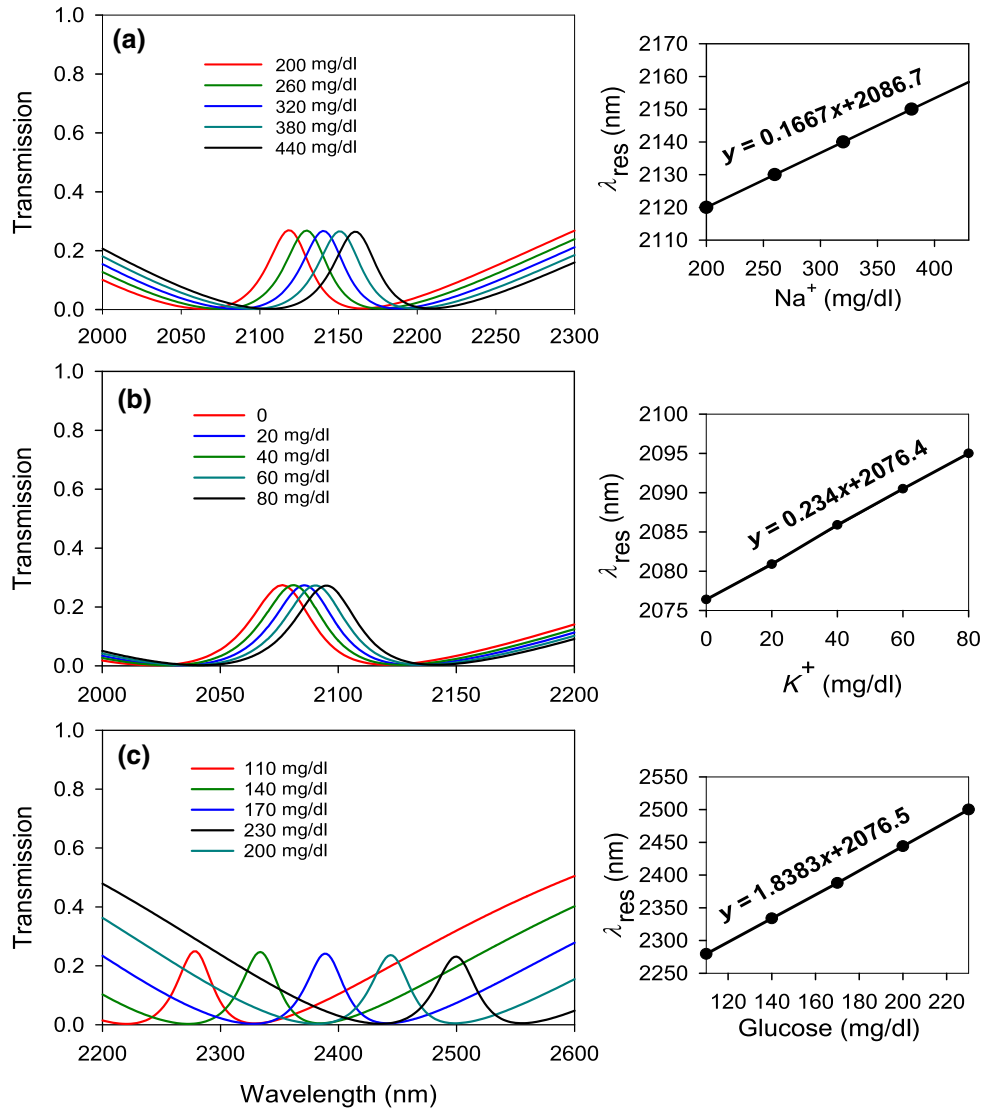

FIG. 8.   Transmission spectra versus the wavelength for different concentration C of (a) Na^+, (b) K^+, and (c) glucose solution. Change of the peaks' wavelength versus the concentrations are presented in the insets of (a),(b),(c), respectively.

a simple device that can be miniaturized at the nanoscale. Indeed, the compact design of the sensor makes it suitable to be integrated into the on-chip optical sensing platforms.

V. CONCLUSION

In this paper, we have given an analytical demonstration of FW BICs and induced resonances in a simple T-shaped cavity with both an experimental evidence in the radiofrequency domain using coaxial cables and a numerical validation in the infrared domain using nanometric M-I-M waveguides with an application for gaz sensing and biosensing. The cavity is made of two horizontal guides of lengths d_2 and d_3 coupled to a vertical guide of length d_1. We have demonstrated analytically that the FW BICs are obtained by choosing d_2 and d_3 commensurate at certain frequencies, which are independent of d_1 and of the infinite waveguide. These BICs are common modes of the guides d_2 and d_3, such as the electric field vanishes at their connection point with the stub of length d_1. Therefore, they are modes of both closed T-shaped cavities with Neumann or Dirichlet boundary conditions at the bottom side of d_1. We have shown that the FW BICs appear as a consequence of the interaction between two DBCS (or two NBCS) branches. The coupling strength between the two branches depends strongly on d_1. In addition, we have shown that by slightly shifting from the BIC condition, this latter transforms into either EIT-EIR or ATS resonances with a finite width. EIT and ATS resonances show similar behaviors in the transmission spectra. However, in order to discern between them, first we have fitted the two phenomena with the corresponding fitting formula. Then, we have used an AIC test to select the best fitting model for each resonance and discriminate the regime where EIT or ATS dominates as a function of δ. Also, we have given a comparison between the DOS and the derivative of the argument of the determinant of the scattering matrix (the Friedel phase [66]), which can be measured experimentally. Furthermore, we have transposed our analytical results to M-I-M plasmonic waveguides operating in the infrared domain. These results are validated by numerical simulation using the finite-element method based on COMSOL Multiphysics software. Finally, we have shown that the T cavity can be used as a sensor with a good sensitivity to detect both the gaz or the concentrations Na^+, K^+ and glucose solutions in comparison with other plasmonic sensors [48,67–74]. Finally, the compact design of the sensor makes it suitable to be integrated into the on-chip optical sensing platforms.

Let us mention that the validity of our results is subject to the requirement that the propagation is monomode, namely, the cross-section size of the waveguides is small enough compared to their lengths and to the propagation wavelength. In the case of multimode circuits with high-order modes, our analytical results are no longer valid

and a numerical treatment is required. In such a study, multiple periods of field in the transverse cross section should be considered above the cutoff frequency. BICs in waveguides with large transverse cross sections have been addressed in acoustics and photonics by introducing discontinuities inside the waveguides [89–91]. The authors of these papers explain that these BICs occur when they belong to different symmetries of the system.

---

[1] C. W. Hsu, B. Zhen, A. D. Stone, J. D. Joannopoulos, and M. Soljačić, Bound states in the continuum, Nat. Rev. Mater. **1,** 16048 (2016).

[2] J. Von Neumann and E. P. Wigner, Uber merkwiirdige diskrete Eigenwerte, Phys. Z. **30,** 465 (1929).

[3] A. A. Bogdanov, K. L. Koshelev, P. V. Kapitanova, M. V. Rybin, S. A. Gladyshev, Z. F. Sadriev, K. B. Samusev, Y. S. Kivshar, and M. F. Limonov, Bound states in the continuum and Fano resonances in the strong mode coupling regime, Adv. Photonics **1,** 016001 (2019).

[4] Q. Mi, T. Sang, Y. Pei, C. Yang, S. Li, Y. Wang, and B. Ma, High-quality-factor dual-band Fano resonances induced by dual bound states in the continuum using a planar nanohole slab, Nanoscale Res. Lett. **16,** 150 (2021).

[5] S. I. Azzam and A. V. Kildishev, Photonic bound states in the continuum: From basics to applications, Adv. Opt. Mater. **9,** 2001469 (2021).

[6] S. Sun, Y. Ding, H. Li, P. Hu, C.-W. Cheng, Y. Sang, F. Cao, Y. Hu, A. Alu, D. Liu, Z. Wang, S. Gwo, D. Han, and J. Shi, Tunable plasmonic bound states in the continuum in the visible range, Phys. Rev. B **103,** 045416 (2021).

[7] Z. Qi, G. Hu, B. Liu, Y. Li, C. Deng, P. Zheng, F. Wang, L. Zhao, and Y. Cui, Plasmonic nanocavity for obtaining bound state in the continuum in silicon waveguides, Opt. Express **29,** 9312 (2021).

[8] A. A. Lyapina, D. N. Maksimov, A. S. Pilipchuk, and A. F. Sadreev, Bound states in the continuum in open acoustic resonators, J. Fluid Mech. **780,** 370 (2015).

[9] L. Huang, Y. K. Chiang, S. Huang, C. Shen, F. Deng, Y. Cheng, B. Jia, Y. Li, D. A. Powell, and A. E. Miroshnichenko, Sound trapping in an open resonator, Nat. Commun **12,** 4819 (2021).

[10] M. Amrani, I. Quotane, C. Ghouila-Houri, E. H. El Boudouti, L. Krutyansky, B. Piwakowski, P. Pernod, A. Talbi, and B. Djafari-Rouhani, Experimental evidence of the existence of bound states in the Continuum and Fano resonances in solid-liquid layered media, Phys. Rev. Appl. **15,** 054046 (2021).

[11] S. T. Ha, Y. H. Fu, N. K. Emani, Z. Pan, R. M. Bakker, R. Paniagua-Domínguez, and A. I. Kuznetsov, Directional lasing in resonant semiconductor nanoantenna arrays, Nat. Nanotechnol. **13,** 1042 (2018).

[12] S. Joseph, S. Pandey, S. Sarkar, and J. Joseph, Bound states in the continuum in resonant nanostructures: An overview of engineered materials for tailored applications, Nanophotonics **10,** 4175 (2021).

[13] S. Weimann, Y. Xu, R. Keil, A. E. Miroshnichenko, A. Tünnermann, S. Nolte, A. A. Sukhorukov, A. Szameit, and Y. S.

Kivshar, Compact surface fano states embedded in the continuum of waveguide arrays, Phys. Rev. Lett. **111**, 240403 (2013).

[14] S. Li, C. Zhou, T. Liu, and S. Xiao, Symmetry-protected bound states in the continuum supported by all-dielectric metasurfaces, Phys. Rev. A **100**, 063803 (2019).

[15] Z. F. Sadrieva, M. A. Belyakov, M. A. Balezin, P. V. Kapitanova, E. A. Nenasheva, A. F. Sadreev, and A. A. Bogdanov, Experimental observation of a symmetry-protected bound state in the continuum in a chain of dielectric disks, Phys. Rev. **99**, 053804 (2019).

[16] Y. Plotnik, O. Peleg, F. Dreisow, M. Heinrich, S. Nolte, A. Szameit, and M. Segev, Experimental observation of optical bound states in the continuum, Phys. Rev. Lett. **107**, 183901 (2011).

[17] H. Friedrich and D. Wintgen, Interfering resonances and bound states in the continuum, Phys. Rev. A **32**, 3231 (1985).

[18] A. F. Sadreev, E. N. Bulgakov, and I. Rotter, Bound states in the continuum in open quantum billiards with a variable shape, Phys. Rev. B **107**, 235342 (2006).

[19] M. Amrani, S. Khattou, E. H. El Boudouti, A. Talbi, A. Akjouj, L. Dobrzynski, and B. Djafari-Rouhani, Friedrich-Wintgen bound states in the continuum and induced resonances in a loop laterally coupled to a waveguide, Phys. Rev. B **106**, 125414 (2022).

[20] N. Solodovchenko, K. Samusev, D. Bochek, and M. Limonov, Bound states in the continuum in strong-coupling and weak-coupling regimes under the cylinder-ring transition, Nanophotonics **10**, 4347 (2021).

[21] L. Huang, L. Xu, M. Rahmani, D. Neshev, and A. E. Miroshnichenko, Pushing the limit of high-Q mode of a single dielectric nanocavity, Adv. Photonics **3**, 016004 (2021).

[22] M. V. Rybin, K. L. Koshelev, Z. F. Sadrieva, K. B. Samusev, A. A. Bogdanov, M. F. Limonov, and Y. S. Kivshar, High-Q supercavity modes in subwavelength dielectric resonators, Phys. Rev. Lett. **119**, 243901 (2017).

[23] L. Huang, B. Jia, A. S. Pilipchuk, Y. Chiang, S. Huang, J. Li, C. Shen, E. N. Bulgakov, F. Deng, D. A. Powell, and S. A. Cummer, General framework of bound states in the continuum in an open acoustic resonator, Phys. Rev. Appl. **18**, 054021 (2022).

[24] U. Fano, Effects of configuration interaction on intensities and phase shifts, Phys. Rev. **124**, 1866 (1961).

[25] A. E. Miroshnichenko, S. Flach, and Y. S. Kivshar, Fano resonances in nanoscale structures, Rev. Mod. Phys. **82**, 2257 (2010).

[26] S. E. Harris, Electromagnetically induced transparency, Phys. Today **50**, 36 (1997).

[27] T. Mrabti, Z. Labdouti, A. Mouadili, E. H. El Boudouti, and B. Djafari-Rouhani, Aharonov-Bohm-effect induced transparency and reflection in mesoscopic rings side coupled to a quantum wire, Physica E Low Dimens. Syst. Nanostruct. **116**, 113770 (2020).

[28] S. H. Autler and C. H. Townes, Stark effect in rapidly varying fields, Phys. Rev. **100**, 703 (1955).

[29] B. Peng, S. K. Ozdemir, Chen, F. Nori, and L. Yang, What is and what is not electromagnetically induced transparency in whispering-gallery microcavities, Nat. Commun. **5**, 5082 (2014).

[30] G. Breit and E. Wigner, Capture of slow neutrons, Phys. Rev. **49**, 519 (1936).

[31] M. Luo, Y. Zhou, X. Zhao, Y. Li, Z. Guo, X. Yang, M. Zhang, Y. Wang, and X. Wu, Label-free bound-states-in-the-continuum biosensors, Biosensors **12**, 1120 (2022).

[32] D. N. Maksimov, V. S. Gerasimov, S. Romano, and S. P. Polyutov, Refractive index sensing with optical bound states in the continuum, Opt. Express **28**, 38907 (2020).

[33] S. Mesli, H. Yala, M. Hamidi, A. BelKhir, and F. I. Baida, High performance for refractive index sensors via symmetry-protected guided mode resonance, Opt. Express **29**, 21199 (2021).

[34] D. N. Maksimov, V. S. Gerasimov, A. A. Bogdanov, and S. P. Polyutov, Enhanced sensitivity of an all-dielectric refractive index sensor with an optical bound state in the continuum, Phys. Rev. A **105**, 033518 (2022).

[35] S. Romano, A. Lamberti, M. Masullo, E. Penzo, S. Cabrini, I. Rendina, and V. Mocella, Optical biosensors based on photonic crystals supporting bound states in the continuum, Materials **11**, 526 (2018).

[36] Q. Wang, J. X. Jiang, L. Wang, X. Y. Yin, X. Yan, A. Zhu, F. Qiu, and K. K. Zhang, An asymmetric grating refractive index sensor generating quasi-bound states in the continuum with high figure of merit and temperature self-compensation, J. Phys. D: Appl. Phys. **55**, 155103 (2022).

[37] Y. K. Srivastava, R. T. Ako, M. Gupta, M. Bhaskaran, S. Sriram, and R. Singh, Terahertz sensing of 7 nm dielectric film with bound states in the continuum metasurfaces, Appl. Phys. Lett. **115**, 151105 (2019).

[38] T. C. Tan, Y. K. Srivastava, R. T. Ako, W. H. Wang, M. Bhaskaran, S. Sriram, I. Al-Naib, E. Plum, and R. Singh, Active control of nanodielectric-induced THz quasi-BIC in flexible metasurfaces: A platform for modulation and sensing, J. Adv. Mater. **33**, 2100836 (2021).

[39] H. Chen, H. Wang, K. Y. Wong, and D. Lei, High-Q localized surface plasmon resonance based on bound states in the continuum for enhanced refractive index sensing, J. Opt. Lett. **47**, 609 (2022).

[40] S. Tang, C. Chang, P. Zhou, and Y. Zou, Numerical study on a bound state in the continuum assisted plasmonic refractive index sensor, Photonics **9**, 224 (2022).

[41] W. Liu, W. Li, C. Liu, E. Xing, Zhou, L. Liu, Y. Shi, and J. Tang, All-optical tuning of Fano resonance for quasi-BIC and terahertz sensing applications, Appl. Sci. **12**, 4207 (2022).

[42] N. L. Kazanskiy, S. N. Khonina, and M. A. Butt, Plasmonic sensors based on Metal-insulator-metal waveguides for refractive index sensing applications: A brief review, Physica E Low Dimens. Syst. Nanostruct. **117**, 113798 (2020).

[43] R. Adhikari, D. Chauhan, G. T. Mola, and R. P. Dwivedi, A review of the current state-of-the-art in Fano resonance-based plasmonic metal-insulator-metal waveguides for sensing applications, Opto-Electron. Rev. **29**, 148 (2021).

[44] R. Al Mahmud, R. H. Sagor, and M. Z. M. Khan, Surface plasmon refractive index biosensors: A review of optical fiber, multilayer 2D material and gratings, and MIM configurations, Opt. Laser Technol. **159**, 108939 (2023).

[45] Z. Chen, L. Yu, L. Wang, G. Duan, Y. Zhao, and J. Xiao, A refractive index nanosensor based on Fano resonance in the plasmonic waveguide system, IEEE Photon. Technol. Lett. **27,** 1695 (2015).

[46] S. Rohimah, H. Tian, J. Wang, J. Chen, J. Li, X. Liu, J. Cui, and Y. Hao, Tunable multiple Fano resonances based on a plasmonic metal-insulator-metal structure for nano-sensing and plasma blood sensing applications, Appl. Opt. **61,** 1275 (2022).

[47] R. Pei, D. Liu, Q. Zhang, Z. Shi, Y. Sun, X. Liu, and J. Wang, Fluctuation of plasmonically induced transparency peaks within multi-rectangle resonators, Sensors **23,** 226 (2022).

[48] J. Chen, X. Lian, M. Zhao, and C. Xie, Multimode Fano resonances sensing based on a non-through MIM waveguide with a square split-ring resonance cavity, Biosensors **12,** 306 (2022).

[49] A. E. Cetin and H. Altug, Fano resonant ring/disk plasmonic nanocavities on conducting substrates for advanced biosensing, ACS Nano **6,** 9989 (2012).

[50] X. Wang, C. Santschi, and O. J. Martin, Strong Improvement of long-term chemical and thermal stability of plasmonic silver nanoantennas and films, Small **13,** 1700044 (2017).

[51] Z. Chai, X. Hu, Y. Zhu, S. Sun, H. Yang, and Q. Gong, Ultracompact chip-integrated electromagnetically induced transparency in a single plasmonic composite nanocavity, Adv. Opt. Mater. **2,** 320 (2014).

[52] X. Yang, X. Hu, H. Yang, and Q. Gong, Ultracompact all-optical logic gates based on nonlinear plasmonic nanocavities, Nanophotonics **6,** 365 (2017).

[53] Z. Chai, X. Hu, H. Yang, and Q. Gong, Chip-integrated all-optical diode based on nonlinear plasmonic nanocavities covered with multicomponent nanocomposite, Nanophotonics **6,** 329 (2017).

[54] S. Kamada, T. Okamoto, S. E. El-Zohary, and M. Haraguchi, Design optimization and fabrication of Mach-Zehnder interferometer based on MIM plasmonic waveguides, Opt. Express **24,** 16224 (2016).

[55] T. Zhou, X. Gou, W. Xu, Y. Li, X. Zhai, H. Li, and L. Wang, Dynamically tunable plasmon-induced transparency in a T-shaped cavity waveguide based on bulk Dirac semimetals, Plasmonics **16,** 323 (2021).

[56] B. Yun, G. Hu, and Y. Cui, Systematical research on the plasmon-induced transparency in coupled plasmonic resonators, Opt. Commun. **305,** 17 (2013).

[57] Z. Han and S. I. Bozhevolnyi, Plasmon-induced transparency with detuned ultracompact Fabry-Perot resonators in integrated plasmonic devices, Opt. Express **19,** 3251 (2011).

[58] M. Kamari, M. Hayati, and S. Khosravi, Tunable infrared wide band-stop plasmonic filter using T-shaped resonators, Mater. Sci. Semicond. **133,** 105983 (2021).

[59] H. Bahri, S. Mouetsi, A. Hocini, and H. Ben Salah, A high sensitive sensor using MIM waveguide coupled with a rectangular cavity with Fano resonance, Opt. Quantum Electron. **53,** 1 (2021).

[60] L. Wang, Y. P. Zeng, Z. Y. Wang, X. P. Xia, and Q. Q. Liang, A refractive index sensor based on an analogy T shaped metal-insulator-metal waveguide, Optik **172,** 1199 (2018).

[61] L. Dobrzynski, A. Akjouj, E. H. El Boudouti, G. Lévêque, H. Al-Wahsh, Y. Pennec, C. Ghouila-Houri, A. Talbi, B. Djafari-Rouhani, and Y. Jin, *Photonics Part II,* (Elsevier, Amsterdam, 2020).

[62] A. Mouadili, E. H. El Boudouti, A. Soltani, A. Talbi, B. Djafari-Rouhani, A. Akjouj, and K. Haddadi, Electromagnetically induced absorption in detuned stub waveguides: A simple analytical and experimental model, J. Condens. Matter Phys. **26,** 505901 (2014).

[63] J. Liu, H. Yang, C. Wang, K. Xu, and J. Xiao, Experimental distinction of Autler-Townes splitting from electromagnetically induced transparency using coupled mechanical oscillators system, Sci. Rep. **6,** 19040 (2016).

[64] L. Giner, L. Veissier, B. Sparkes, A. S. Sheremet, A. Nicolas, O. S. Mishina, M. Scherman, S. Burks, I. Shomroni, D. V. Kupriyanov, and P. K. Lam, Experimental investigation of the transition between Autler-Townes splitting and electromagnetically-induced-transparency models, Phys. Rev. A **87,** 013823 (2013).

[65] P. M. Anisimov, J. P. Dowling, and B. C. Sanders, Objectively discerning autler-townes splitting from electromagnetically induced transparency, Phys. Rev. Lett. **107,** 163604 (2011).

[66] J. Friedel, The distribution of electrons round impurities in monovalent metals, Philos. Mag. **43,** 153 (1952).

[67] M. F. Hassan, R. H. Sagor, M. R. Amin, M. R. Islam, and M. S. Alam, Point of care detection of blood electrolytes and glucose utilizing nano-dot enhanced plasmonic biosensor, IEEE Sens. J. **21,** 17749 (2021).

[68] Y. Shubin, L. Pengwei, C. Zhanbo, L. Jilai, S. Lifang Shen, Z. Xiaoyu, C. Jiaming, L. Tingsong, C. Yang, and R. Yifeng, High-property refractive index and bio-sensing dual-purpose sensor based on SPPs, Micromachines **13,** 846 (2022).

[69] T. Li, S. Yan, P. Liu, X. Zhang, Y. Zhang, L. Shen, Y. Ren, and E. Hua, A nanoscale structure based on an MIM waveguide coupled with a Q resonator for monitoring trace element concentration in the human body, Micromachines **12,** 1384 (2021).

[70] J. Chen, Z. Li, Y. Zou, Z. Deng, J. Xiao, and Q. Gong, Coupled-resonator-induced Fano resonances for plasmonic sensing with ultra-high figure of merits, Plasmonics **8,** 1627 (2013).

[71] Z. Q. Chen, J. W. Qi, J. Chen, Y. D. Li, Z. Q. Hao, W. Q. Lu, J. J. Xu, and Q. Sun, Fano resonance based on multimode interference in symmetric plasmonic structures and its applications in plasmonic nanosensors, Chin. Phys. Lett. **30,** 057301 (2013).

[72] Z. Chen, X. Song, R. Jiao, G. Duan, L. Wang, and L. Yu, Tunable electromagnetically induced transparency in plasmonic system and its application in nanosensor and spectral splitting, IEEE Photon. J. **7,** 1 (2015).

[73] Z. Chen and L. Yu, Multiple Fano resonances based on different waveguide modes in a symmetry breaking plasmonic system, IEEE Photon. J. **6,** 1 (2014).

[74] R. Zafar and M. Salim, Enhanced figure of merit in Fano resonance-based plasmonic refractive index sensor, IEEE Sens. J. **15,** 6313 (2015).

[75] J. O. Vasseur, A. Akjouj, L. Dobrzynski, B. Djafari-Rouhani, and E. H. El Boudouti, Photon, electron, magnon,

phonon and plasmon mono-mode circuits, Surf. Sci. Rep. **54**, 1 (2004).

[76] See Supplemental Material at http://link.aps.org/supplemental/10.1103/PhysRevApplied.20.044015 for the details of the analytical calculations of the transmission and reflections coefficients through the T-shaped cavity (SM1), Friedrich-Wintgen BICs resulting from the interaction between two NBCS branches (SM2), the effect of the guide of length d_1 on the BIC and EIR resonance (SM3), distinction between EIT and ATS resonances using an Akaike information criterion test (SM4), the approximate results around two interacting DBCS modes (SM5), numerical and experimental comparison between the variation of the density of states and the first derivative of the Friedel phase (SM6), the evolution of the coupling strengths between two DBCS modes or two NBCS modes as a function of d_1 (SM7), and numerical results for gold (instead of silver) as metal (SM8).

[77] B. Djafari-Rouhani, E. H. El Boudouti, A. Akjouj, L. Dobrzynski, J. O. Vasseur, A. Mir, N. Fettouhi, and J. Zemmouri, Surface states in one-dimensional photonic band gap structures, Vacuum **63**, 177 (2001).

[78] S. Khattou, M. Amrani, A. Mouadili, A. Talbi, A. Akjouj, and B. Djafari-Rouhani, Comparison of density of states and scattering parameters in coaxial photonic crystals: Theory and experiment, Phys. Rev. B **102**, 165310 (2020).

[79] S. A. Maier, *Plasmonics: Fundamentals and Applications,* (Springer, Berlin, 2007).

[80] M. Zhang and Z. Wang, Analytical method for metal-insulator-metal surface plasmon polaritons waveguide networks, Opt. Express **27**, 3 (2019).

[81] Z. Qiong-Gan and W. Zhi-Guo, The Green's function method for metal-dielectric-metal SPP waveguide network, Europhys. Lett. **103**, 17004 (2013).

[82] P. B. Johnson and R. W. Christy, Optical constants of the noble metals, Phys. Rev. B **6**, 4370 (1972).

[83] S. Naghizadeh and S. E. Kocabas, Guidelines for designing 2D and 3D plasmonic stub resonators, J. Opt. Soc. Am. B **34**, 207 (2017).

[84] M. R. Rakhshani and M. A. Mansouri-Birjandi, High-sensitivity plasmonic sensor based on metal-insulator-metal waveguide and hexagonal-ring cavity, IEEE Sens. J. **16**, 3041 (2016).

[85] M. Amrani, S. Khattou, Y. Rezzouk, A. Mouadili, A. Noual, E. H. El Boudouti, and B. Djafari-Rouhani, Analytical and numerical study of T-shaped plasmonic demultiplexer based on Fano and induced transparency resonances, J. Phys. D: Appl. Phys. **55**, 075106 (2021).

[86] J. Becker, A. Trugler, A. Jakab, U. Hohenester, and C. Sonnichsen, The optimal aspect ratio of gold nanorods for plasmonic bio-sensing, Plasmonics **5**, 161-167 (2010).

[87] C. Y. Tan and Y. X. Huang, Dependence of refractive index on concentration and temperature in electrolyte solution, polar solution, nonpolar solution, and protein solution, J. Chem. Eng. Data **60**, 2827 (2015).

[88] R. R. Singh, S. Kumari, A. Gautam, and V. Priye, Glucose sensing using slot waveguide-based SOI ring resonator, IEEE J. Sel. Top. Quantum Electron. **25**, 1 (2015).

[89] S. Hein and W. Koch, Acoustic resonances and trapped modes in pipes and tunnels, J. Fluid Mech. **605**, 401 (2008).

[90] M. Chao, Q. Liu, W. Zhang, L. Zhuang, and G. Song, Mutual coupling of corner-localized quasi-BICs in high-order topological PhCs and sensing applications, Opt. Express **30**, 29258 (2022).

[91] J. Chen, Q. Cheng, W. Yuan, L. Wang, W. X. Tang, L. Wang, and T. J. Cui, Generation of high-order waveguide modes with reduced symmetric protection, Phys. Rev. Appl. **14**, 024040 (2020).